Support Vector Machine Algorithm for Mapping Land Cover Dynamics in Senegal, West Africa, Using Earth Observation Data

Polina Lemenkova

earth

MDPI

Article

Support Vector Machine Algorithm for Mapping Land Cover Dynamics in Senegal, West Africa, Using Earth Observation Data

Polina Lemenkova [1,2]

[1] Department of Geoinformatics, Faculty of Digital and Analytical Sciences, Paris Lodron Universität Salzburg, Schillerstraße 30, A-5020 Salzburg, Austria; polina.lemenkova@plus.ac.at or polina.lemenkova2@unibo.it; Tel.: +43-677-6173-2772 or +39-344-69-28-732

[2] Department of Biological, Geological and Environmental Sciences, Alma Mater Studiorum—Università di Bologna, Via Irnerio 42, IT-40126 Bologna, Italy

Abstract: This paper addresses the problem of mapping land cover types in Senegal and recognition of vegetation systems in the Saloum River Delta on the satellite images. Multi-seasonal landscape dynamics were analyzed using Landsat 8-9 OLI/TIRS images from 2015 to 2023. Two image classification methods were compared, and their performance was evaluated in the GRASS GIS software (version 8.4.0, creator: GRASS Development Team, original location: Champaign, Illinois, USA, currently multinational project) by means of unsupervised classification using the k-means clustering algorithm and supervised classification using the Support Vector Machine (SVM) algorithm. The land cover types were identified using machine learning (ML)-based analysis of the spectral reflectance of the multispectral images. The results based on the processed multispectral images indicated a decrease in savannas, an increase in croplands and agricultural lands, a decline in forests, and changes to coastal wetlands, including mangroves with high biodiversity. The practical aim is to describe a novel method of creating land cover maps using RS data for each class and to improve accuracy. We accomplish this by calculating the areas occupied by 10 land cover classes within the target area for six consecutive years. Our results indicate that, in comparing the performance of the algorithms, the SVM classification approach increased the accuracy, with 98% of pixels being stable, which shows qualitative improvements in image classification. This paper contributes to the natural resource management and environmental monitoring of Senegal, West Africa, through advanced cartographic methods applied to remote sensing of Earth observation data.

Keywords: remote sensing; cartography; vegetation; West Africa; satellite image; Landsat; Sahel; climate change; landscape; land cover types

PACS: 91.10.Da; 91.10.Jf; 91.10.Sp; 91.10.Xa; 96.25.Vt; 91.10.Fc; 95.40.+s; 95.75.Qr; 95.75.Rs; 42.68.Wt

MSC: 86A30; 86-08; 86A99; 86A04

JEL Classification: Y91; Q20; Q24; Q23; Q3; Q01; R11; O44; O13; Q5; Q51; Q55; N57; C6; C61

Citation: Lemenkova, P. Support Vector Machine Algorithm for Mapping Land Cover Dynamics in Senegal, West Africa, Using Earth Observation Data. *Earth* **2024**, *5*, 420–462. https://doi.org/10.3390/earth5030024

Academic Editor: Hariklia D. Skilodimou and Charles Jones

Received: 6 July 2024
Revised: 4 September 2024
Accepted: 5 September 2024
Published: 6 September 2024

1. Introduction

1.1. Background

Land cover and land use change are widely known as key elements of landscapes. Maps showing classification of land cover types are key data sources for assessment of landscape dynamics and for evaluating environmental trends. Land cover types (or land use types) refer to the physical components of Earth cover that are physically present and visible on the Earth's surface. Compared to land use types, which are defined as landscape patches used by people, land cover types typically represent natural physical characteristics of the Earth's surface in terms of structure, patterns, and components.

Characteristics and features of land cover types are visible on satellite images recorded from space. Therefore, remote sensing (RS) data, such as satellite images, are widely used for land cover change analysis using classification maps that show spatio-temporal changes in land cover/land use patterns. Hence, land cover maps are the background geoinformation products necessary for analysts and decision makers. The use of land cover maps enables the monitoring of environmental changes and evaluation of risks to sustainable development. Therefore, the use of land cover maps is applicable in diverse research and development sectors such as governments, civil engineering, and industrial planning [1].

In monitoring landscape dynamics, remote sensing (RS) data are widely used and applied in environmental mapping with the aim of detecting identical landscape patterns in a time series of images and analyzing changes using recognition of landscape patches. In this regard, there is a strong need for machine-based, automated geospatial data processing and image analysis that turns the technical values of pixels in the satellite images into information that provides knowledge and insights for environmental experts and planners. The identification and recognition of land cover types becomes possible using the analysis and synthesis of remote sensing data, such as spaceborne images. Environmental studies often use such products for landscape analysis, for example, images of Landsat missions.

Major types of satellite images for effective interpretation of the Earth's landscapes include Sentinel 2 Data [2,3], NOAA-AVHRR [4–6], SPOT [7,8], and Landsat [9,10], and the combinations thereof [11]. For instance, the recent Global Land Cover 2000 map was implemented using the analysis of the Vegetation Sensor on board the SPOT-4 satellite image [12]. Another example of such products is presented by the time series of annual global maps of land cover types derived from the ESA Sentinel 2 imagery at 10 m resolution [13]. The Landsat scenes used for landscape mapping include data acquired from its various sensors, such as the Multispectral Scanner (MSS), the Thematic Mapper (TM), the Enhanced Thematic Mapper Plus (ETM+), and the recent product called the Operational Land Imager and Thermal Infrared Sensor (OLI/TIRS).

Certainly, although diverse images can be used in various combination as data sources for landscape interpretation and environmental mapping, the general approach of RS data processing relies on using the values of spectral reflectance obtained as digital numbers (DNs) of pixels on the image scene [14]. The effects of reflectance and absorption of various land cover types in different wavelengths enable the discrimination of major land cover types in the multispectral images: water, land, forests (with various types of vegetation), urban zones, and desert sands [15]. Such information can be extracted from variations in brightness, primary colors (red, green, blue), hue, saturation, and intensity of light. In experimental studies, these phenomena are utilized to assess land–water borders and distinguish them from other land cover types, leading to an improvement in the recognition of the Earth's objects [16]. The information provided by the environmental descriptors can be obtained from the analysis of values of pixels recording spectral reflectance of diverse land cover types. In RS, this can be derived from the combination of different bands of the multispectral imagery, e.g., NIR/Red bands for computing the Normalized Difference Vegetation Index (NDVI) and other vegetation indices [17–20].

1.2. Problem Formulation

One of the challenging problems in identification of land cover types in the satellite images consists of automatic extraction of the reliable features visible in the image scene. This is true especially in terms of highly heterogeneous landscape patches in a complex mosaic of intermittent land cover types [21,22]. In this regard, image processing and analysis for landscape interpretation are fundamental issues in environmental mapping and thematic cartography. Identification of land cover types in the RS data requires diverse image processing techniques, such as classification, clustering, and segmentation. Classifying mixed terrestrial ecoregions typical for Senegal requires advanced methods of image analysis [23]. Senegal's landscape is distinctive because it consists of a complex blend

of diverse, semi-arid landscapes, such as forest–savanna mosaics, which are periodically filled with Sahelian acacia and West Sudanian savannas with diverse tree species, as well as coastal regions with dominant Guinean mangroves [24,25].

The current practice of geographic information system (GIS)-based supervised image processing involves manually marking different features in a landscape, such as regions of interest (ROIs), singular patches, and landscape corridors, because the extraction of features from processed images is difficult [26]. The human factor in landscape assessment involves some concerns about the repeatability and reliability, which suggest the need for the development of automatic methods for image interpretation and object recognition [27–29]. Manual interpretation of land cover types can lead to the misclassification of pixels in the images, which might result in misinterpretation of the selected landscape patches. As mentioned earlier, implementing quantitative data interpretation for prediction and analysis is challenging in African countries where fieldwork data are limited [30]. Therefore, RS-based vegetation mapping and agricultural landscape monitoring are vitally dependent on using satellite data processed with a high level of automation [31,32].

Effective image analysis relies heavily on the type of classifier and the algorithms used for data handling [33]. Another important factor is the quality of imagery for the evaluated region of interest (ROI) in the study area, which includes minimal cloudiness and haze, correct time of image capture and coverage. Finally, image analysis is based on the methodology and approaches used in RS, including data acquisition, preprocessing, description, recognition, classification, segmentation, interpretation, and accuracy analysis. The development of computer-based programming methods has led to the growth of novel image processing methods, which are the primary factors in effectiveness [34–38]. Development of the advanced tools of image processing and related cartographic tasks has resulted in many approaches to utilizing effective methods for automation [39–44]. One of these methods is the machine learning (ML)-based Support Vector Machine (SVM) algorithm used for image analysis and synthesis for interpretation of vegetation patterns [45–48].

In this respect, the research questions formulated in this study are as follows: (1) Can the Support Vector Machine (SVM) ML-based land cover detection method be used with GIS for satellite image analysis? (2) How can the SVM algorithm of ML be employed in geoinformation extracting tasks using scripts? (3) What is the workflow for RS data processing for an effective chain of data handling to perform the necessary tasks during SVM-based image classification? Answering these questions enables us to evaluate the effectiveness of SVM as one of the most powerful ML applications in cartographic tasks and RS data analysis.

1.3. Related Work

Many reports have recently been published illustrating land cover changes in Senegal [49–51], effects of climate change on landscape variability and vegetation communities [52–54], environmental dynamics, and sustainability [55]. Nevertheless, these approaches do not take into account the benefits of programming scripts for satellite image processing. At the same time, using ML methods increases the automation of mapping and the speed of data processing, ensuring the accuracy and objectivity of land cover classification. Indeed, image processing using ML methods such as SVM partitions the image into structured land patches using automatic analysis of spectral reflectance of the pixels. The obtained values of pixels are then assigned into various classes using principles of machine-based vision and pattern recognition. Through this approach, it is easy to visualize and estimate changes in land cover types using images from different years as part of a time series analysis. Additionally, it overcomes the problems with conventional software programs used for image processing, which may include drawbacks in data processing.

A drought period in Africa in the 1970s and 1980s resulted in climate changes that include such consequences as decreased rainfall and precipitation, raised temperatures, and increased evaporation [56,57]. These climate-related processes triggered land cover changes in natural vegetation patterns of Sahel ecoregions that affected cultivated areas

and croplands, increased spots of bare soil, and led to changes in surface water [58,59]. To this point, one of the priorities of image processing methods for environmental landscape analysis is to support land cover monitoring through the interpretation of land cover types using time series analysis. Regular monitoring of the Earth's landscapes enables us to detect environmental changes, land and soil degradation, and variations in vegetation cover [60]. Another essential application of image analysis is monitoring coastal zones to evaluate hydrological changes, to evaluate the extent of river flooding in the delta, to detect soil erosion [61,62], and to monitor the degradation of mangroves and coastal ecosystems [63,64]

1.4. Objective and Motivation

Inspired by the existing examples of the ML methods used to analyze multispectral satellite images in environmental applications, this study integrates advanced cartographic scripting methods with applied techniques of SVM image processing for monitoring landscapes in Senegal; see Figure 1.

Figure 1. Study area with segments of the Landsat images shown on a topographic map of Senegal. Software: GMT. Map source: Author.

The environmental analysis was performed using a series of satellite images evaluated for the period from 2015 to 2023. To this end, we explore the classification approach of SVM, which was employed for RS data processing by the scripting techniques of the Geographic Resources Analysis Support System (GRASS) GIS. The SVM classifier is applied as a widely implemented supervised learning approach. Other advanced deep learning (DL) methods that have been developed recently include such methods as autoencoders, a special type of neural network that operates with dimensional latent representation, and vision transformers, which differentially weigh the significance of each part of the image. Nevertheless, SVM is still a sufficient and effective approach for many remote

sensing (RS) and GIS tasks. Given the availability of SVM in GRASS GIS, this method was employed for the image classification.

The main goal of this study is to map and evaluate changes in diverse land cover types in West Senegal, which include both inner regions and coastal mangrove forests in the delta of the Saloum River; see Figure 1. To achieve this goal, the practical objective is to classify land cover types in the coastal region of West Senegal using a series of Landsat 8-9 OLI/TIRS multispectral satellite images processed using ML methods, including SVM as an advanced method of automated image classification. Contrary to the existing GIS, the programming approach to satellite image processing has a high automation in data handling. Additionally, it is a very fast and robust approach for classifying and comparing satellite images. This is achieved by a combination of the embedded GRASS GIS modules is used separately for computing vegetation indices and plotting the classification maps.

According to recent studies, mangrove habitats are drastically disappearing. This is because these ecosystems are being impacted by anthropogenic activity, climate change, and local effects of salinity in the soil [65,66]. By evaluating gains and losses in landscape patches, RS data can be spatially analyzed to understand the dynamics of these distinct wetland ecosystems. Our comprehension of the changes in Senegalese landscapes is aided by satellite image analysis, which shows how these landscapes respond to the effects of West Africa's changing climate, including rising temperatures, evaporation, and falling precipitation.

The goal of using the GRASS GIS scripts for RS data analysis is to quantitatively evaluate changes in land cover types in Senegal as a result of climate fluctuations during a recent eight-year period. The approach to achieve this goal is based on using automated unsupervised classification and supervised classification using the ML method of SVM. In this way, the maximal likelihood and SVM classification algorithms present an effective means by which the Landsat scenes can be processed automatically. The RS data obtained from the United States Geological Survey (USGS) repository were used for environmental analysis and monitoring to evaluate and visualize variations in landscape patches. This analysis is technically based on the ML-based estimation of spectral reflectance on the satellite images, which supports environmental monitoring of the West African landscapes responding to climate and anthropogenic effects.

The main purpose of this paper is to provide an advanced approach using ML to RS data analysis and processing. Such an approach can evaluate the nonlinear behavior of the landscapes in West Africa over time, which indicates the development of climate settings and the related response of vegetation patterns. To this end, we propose a script-based classification and image enhancement technique using GRASS GIS software to analyze land cover changes in the coastal region of West Senegal. This technique aims to address the main challenges associated with traditional image processing, such as structured noise in the classified scenes, poor quality of the images, the misinterpretation of pixels, and the low speed of data handling.

The ML-based image analysis is based on using the RS data, which serve as a cartographic basis to support optimized decisions made by environmental policy makers and planners. Satellite images processed by the machine-based methods allow for the identification of vulnerable landscapes and enable the monitoring of degraded lands in Senegal. In order to do this, a series of the multispectral satellite images from Landsat with recent OLI/TIRS sensors taken on different years was processed with various modules of GRASS GIS. This time series data analysis enabled us to perform an environmental analysis for monitoring landscape dynamics in Senegal.

Importantly, the study presented here is not intended to suggest that scripting methods replace the role of conventional GIS. In contrast, the programming codes supplement the traditional cartographic methods used in the RS software. However, the integration of a scripting workflow with image analysis and cartographic tasks provides an effective approach by which the analysis of land cover changes can be visualized in an automatic way. In light of this, the main contributions of this paper are as follows:

- A combination of the GRASS GIS modules 'i.group', 'i.maxlik', and 'i.cluster' are proposed for the unsupervised image classification. The land cover types are classified based on the difference in spectral reflectance of the pixels in each of the images.
- A set of GRASS GIS modules, including 'r.learn.predict', 'r.learn.train', and 'r.random', is used for supervised ML-based image classification using an SVM modeling algorithm.
- The land cover types in coastal Senegal are defined as groups of pixels according to the structural similarity between the landscape patches. Orientation, location, and frequency of mangrove fields in the Saloum River Delta are estimated from the analysis of landscape patches in the coastal area.
- To balance the robustness and accuracy, a coarse-to-fine strategy is proposed using the interpretation of landscape patches according to the FAO scheme of land cover types. The data for the whole country were downscaled to the ROI of the selected study area, with images covering the region of Cape Verde Peninsula and the surrounding territories.
- The proposed image processing and ML-based classification algorithms utilizing the SVM techniques of GRASS GIS outperform the existing traditional software with graphical user interface (GUI) approaches in terms of repeatability of scripts and automation through computer vision. This methodological workflow is useful for future similar studies of land cover type analysis in Senegal or surrounding areas of West Africa.

2. Materials and Methods

To increase the speed and accuracy of image processing, the GRASS GIS software was applied for advanced image processing due to its extended functionalities [67]. Generic Mapping Tools (GMT) Version 6 [68] was used as a cartographic tool for topography, and RS tasks are based on scripting techniques. The main advantages of scripts include their high speed of data processing and repeatability [69–71].

2.1. Data

We use six Landsat 8-9 OLI/TIRS images for evaluation of land cover changes in western Senegal from 2015 to 2023. Major metadata are summarized in Table 1.

Table 1. Identifiers (IDs) of the six multispectral Landsat 8-9 OLI/TIRS images.

Date	Landsat Product Identifier L1	Landsat Product Identifier L2	Scene ID
25 February 2015	LC08_L1TP_205050_20150225_20200909_02_T1	LC08_L2SP_205050_20150225_20200909_02_T1	LC82050502015056LGN01
17 February 2018	LC08_L1TP_205050_20180217_20200902_02_T1	LC08_L2SP_205050_20180217_20200902_02_T1	LC82050502018048LGN00
7 February 2020	LC08_L1TP_205050_20200207_20200823_02_T1	LC08_L2SP_205050_20200207_20200823_02_T1	LC82050502020038LGN00
25 February 2021	LC08_L1TP_205050_20210225_20210304_02_T1	LC08_L2SP_205050_20210225_20210304_02_T1	LC82050502021056LGN00
20 February 2022	LC09_L1TP_205050_20220220_20230427_02_T1	LC09_L2SP_205050_20220220_20230427_02_T1	LC92050502022051LGN01
22 January 2023	LC09_L1TP_205050_20230122_20230313_02_T1	LC09_L2SP_205050_20230122_20230313_02_T1	LC92050502023022LGN01

The images were downloaded from the United States Geological Survey (USGS) EarthExplorer repository; see Figure 2. The data contain scenes taken during the winter period (January/February). The selection of the winter period is explained by the fact that images taken during winter enable us to better detect plant phenology in a semi-arid climate. In contrast, those collected during summer are not suitable for plant detection due to the high level of droughts in the desert areas, especially in the inner regions of the country. Additionally, the images were collected with minimized cloudiness and haze below 10%. Hence, the best quality and suitability of images was in the winter period, during the months of January and February. All Landsat images are multispectral and have a 30 m resolution in visible spectral bands. The images are projected in Universal Transverse Mercator (UTM) Zone 28 for western Senegal. The Landsat images used in this study are presented in Figure 3.

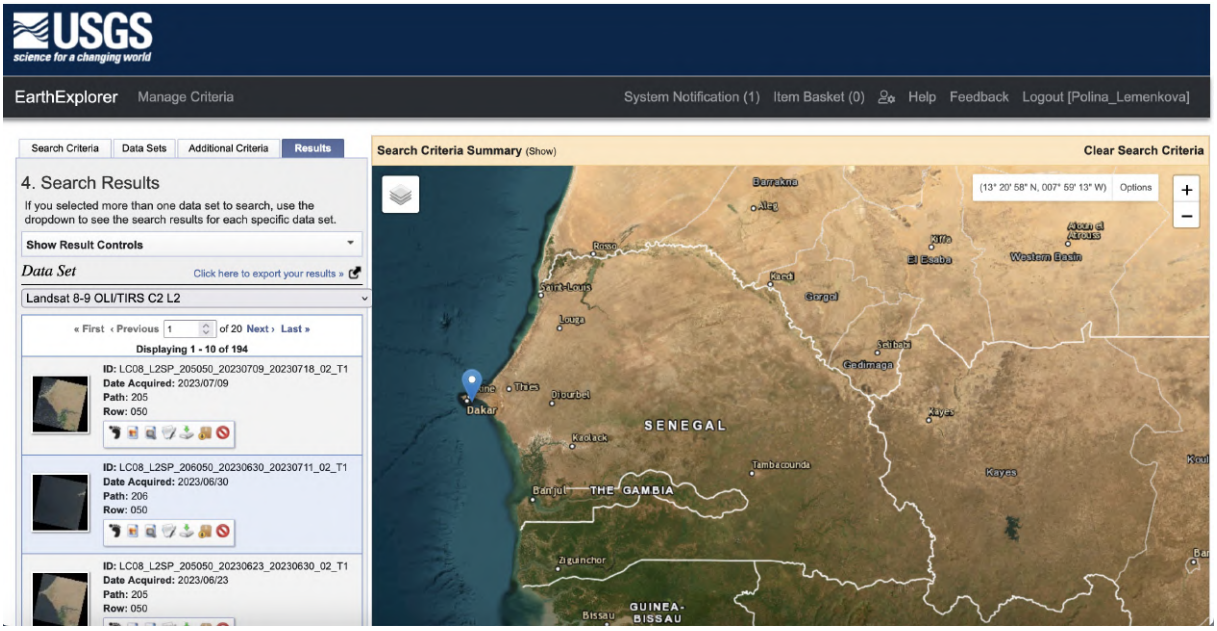

Figure 2. Data capture of Landsat images from the USGS EarthExplorer repository.

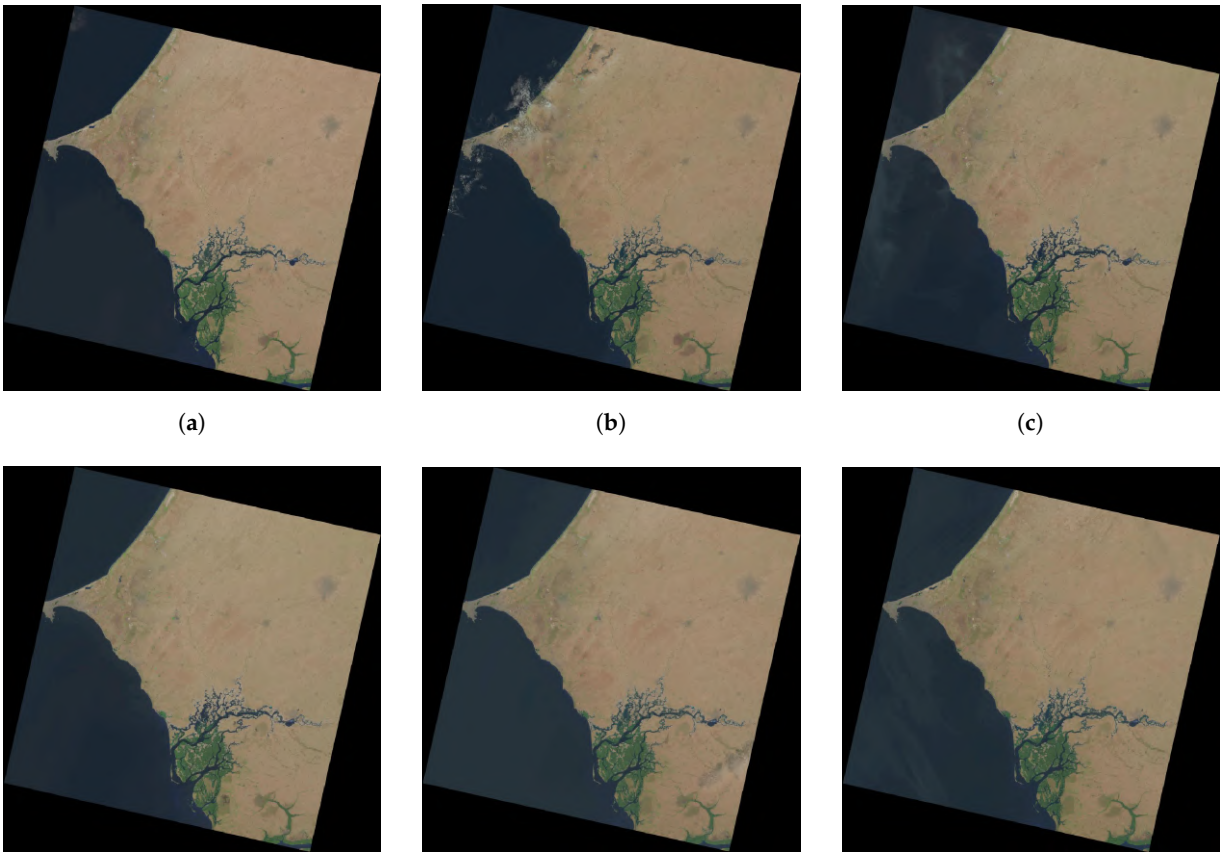

(**a**) (**b**) (**c**)

(**d**) (**e**) (**f**)

Figure 3. Landsat images in RGB colors covering the Cape Verde Peninsula region and Saloum River Delta, West Senegal, in February: (**a**) 2015; (**b**) 2018; (**c**) 2020; (**d**) 2021; (**e**) 2022; (**f**) 2023.

It is well-known that the high-resolution commercial satellite images (e.g., SPOT, Pleiades) are expensive due to the expenses related to the launch of the satellite and related operational costs. Therefore, such scenes are not always easily accessible as a data source. Hence, the use of the open source Landsat 8-9 OLI/TIRS is crucial, and the value of these

products to environmental monitoring is high. This is especially true for replication of this study in future similar work. The aim of the multispectral Landsat images was to examine the impact of both anthropogenic and climatic factors on the process of land cover change in western Senegal. This was achieved by analyzing and processing the spectral reflectance characteristics of the pixels obtained from the RS data.

The images were selected for different years (2015 to 2023) for comparability. Using RS techniques, the environmental characteristics of the landscapes were evaluated in order to analyze how changes in climate are affecting the types of land cover and, in particular, the distribution of mangroves along the Saloum River Delta. The metadata for the images were evaluated for each scene: four images were selected from the Landsat-8 OLI-TIRS sensor, and two recent scenes were selected from the Landsat-9 OLI-TIRS sensor instruments.

2.2. Methodology

The methodology of this study is based on scripting software for data processing. Technically, we propose a novel mapping method using the SVM algorithm in GRASS GIS for improving the image classification task, and we compare it with the conventional method of unsupervised classification using k-means clustering. Major programming scripts are shown in Appendix B for technical reference. The full codes have been placed in a GitHub repository, including ML techniques of SVM). The advantage of the GRASS GIS approach to RS data processing consists of adjusted modules enabling us to analyze spectral properties of the satellite images. Additionally, the GMT was applied for cartographic mapping. This paper presents a series of scripting experiments that utilize both software applications. Methods of applied programming enabled us to evaluate recent dynamics of land cover types in Senegal.

The advanced script-based cartographic methods of monitoring and mapping land cover types are built on a growing demand for time- and cost-effective approaches in cartographic workflow and RS data analysis. Their use enables us to save time and resources while processing large geospatial datasets using satellite images obtained from open sources. Hence, three major script-based tool sets were used in this study for geospatial data analysis and environmental monitoring in West Africa:

1. The GMT script was used for plotting the topography of the country; see Listing A1.
2. An R script was used for plotting the methodological flowchart; see Listing A2.
3. GRASS GIS scripts were used for image processing; see Listings A3 and A4.

The main idea was to apply a single workflow framework for both the image processing and the cartographic mapping tasks using scripts run from the console. This enabled us to reveal the advantages of the technical performance of automated geospatial data processing. More specifically, using a programming approach that includes various programming suites from the script-based software presents a novel workflow for geospatial data processing. This method demonstrates how adding scripts expedites the process of image analysis and cartographic plotting while also providing an overview of the study methods. As mentioned earlier [72], the automation of the cartographic procedure and the workflow's repeatability in future research are the primary benefits of scripts. Moreover, scripting enables us to save significant time due to automation. We were able to identify changes in the analysis of landscapes of western Senegal for the assessment of environmental impacts from climate change by using the information obtained from the automated image analysis and interpretation. This was done by evaluating a series of images and analyzing RS data.

The workflow of the data processing and major methodological steps is shown in Figure 4, with the goal of performing image classification and interpretation in order to detect changes in land cover types. The data processing was technically implemented using GRASS GIS software [73] and run on a Mac machine with Apple M1 chip and the MacOS operating system. After preprocessing and data import, the images were grouped to select the necessary multispectral raster bands for image processing. This was performed by the 'i.group' module of GRASS GIS [74]. Afterwards, the images were clustered using

unsupervised classification. This was carried out utilizing the module 'i.cluster', which automatically assigns pixels into groups according to their spectral reflectance. This method of image processing provided enough data to group the pixels into land cover types and to evaluate the values of pixels in the actual scenes for comparison. The average computation time for image classification and enhancement per Landsat scene is about 2.5 s.

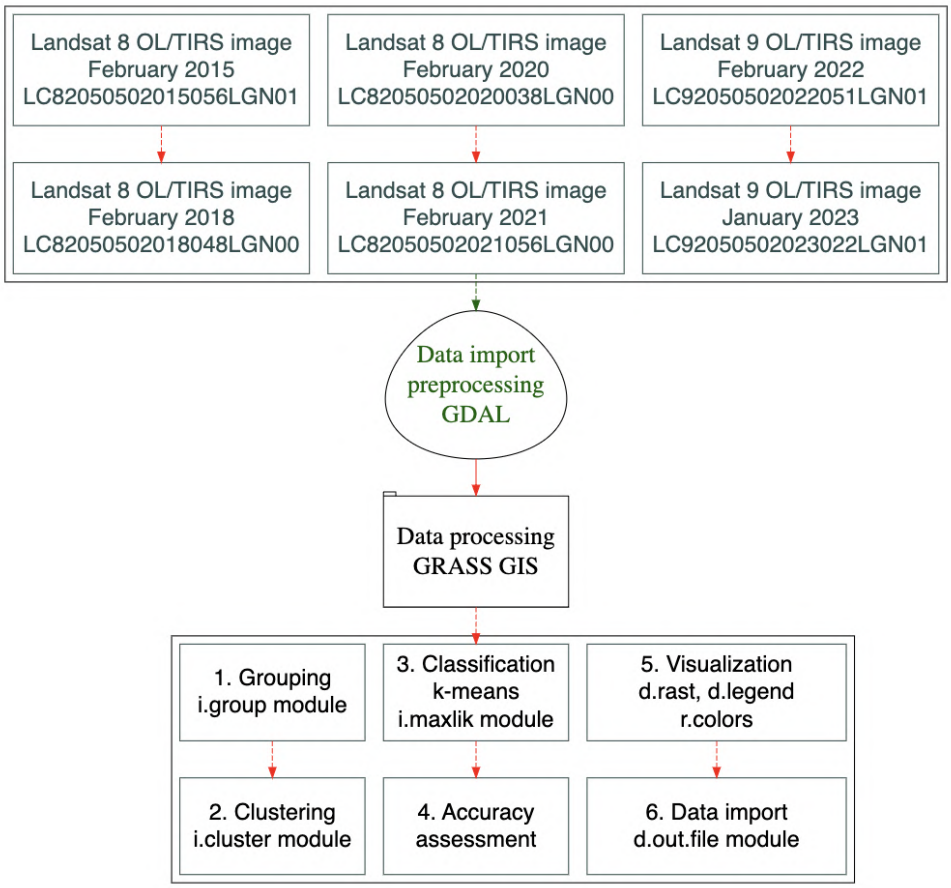

Figure 4. Workflow scheme illustrating the data and the main methodological steps. Software: R version 4.3.3, library DiagrammeR version 1.0.11. Diagram source: Author.

The matching performance of landscape patches over this period is evaluated using GRASS GIS functionality as a sequence of modules utilized for processing each scene separately using a script. The images were read into the GRASS GIS environment using the 'r.import' module; the list of the available bands was checked using the 'g.list rast' command. The extent of the ROI (UTM Zone 28) and the resolution were set to the region of the current image, which was detected automatically along with geospatial data such as coordinates, location, and projection. The false color composites were plotted to distinguish the area of vegetation in the delta of the Saloum River (colored in red shadows), land (colored by beige and light brownish shadows), and water areas (colored black for seawater and navy blue for the Saloum River); see Figure 5.

The ML method of satellite image processing involves using the SVM algorithm for data partition and classification. To perform these steps with fixed ML parameters, we utilize the GRASS GIS modules 'r.random' for generating a training dataset from pixels obtained from the land cover classification, the 'r.learn.train' module for training a Support Vector Classification (SVC) model, and the 'r.learn.predict' module, which predicts the pixel's assignment to the target classes. We represent the image dataset as a time series of scenes from 2015 to 2023 represented as color composites from the multispectral bands of Landsat. We denote the number of estimators as 500 in the model and the number of seed points as 100 pixels, with a total of 1000 evaluated pixels ('npoints' in the model's syntax).

The training model name is explicitly defined as 'SVC', i.e., Support Vector Classification, as it is the algorithm embedded in the GRASS GIS software.

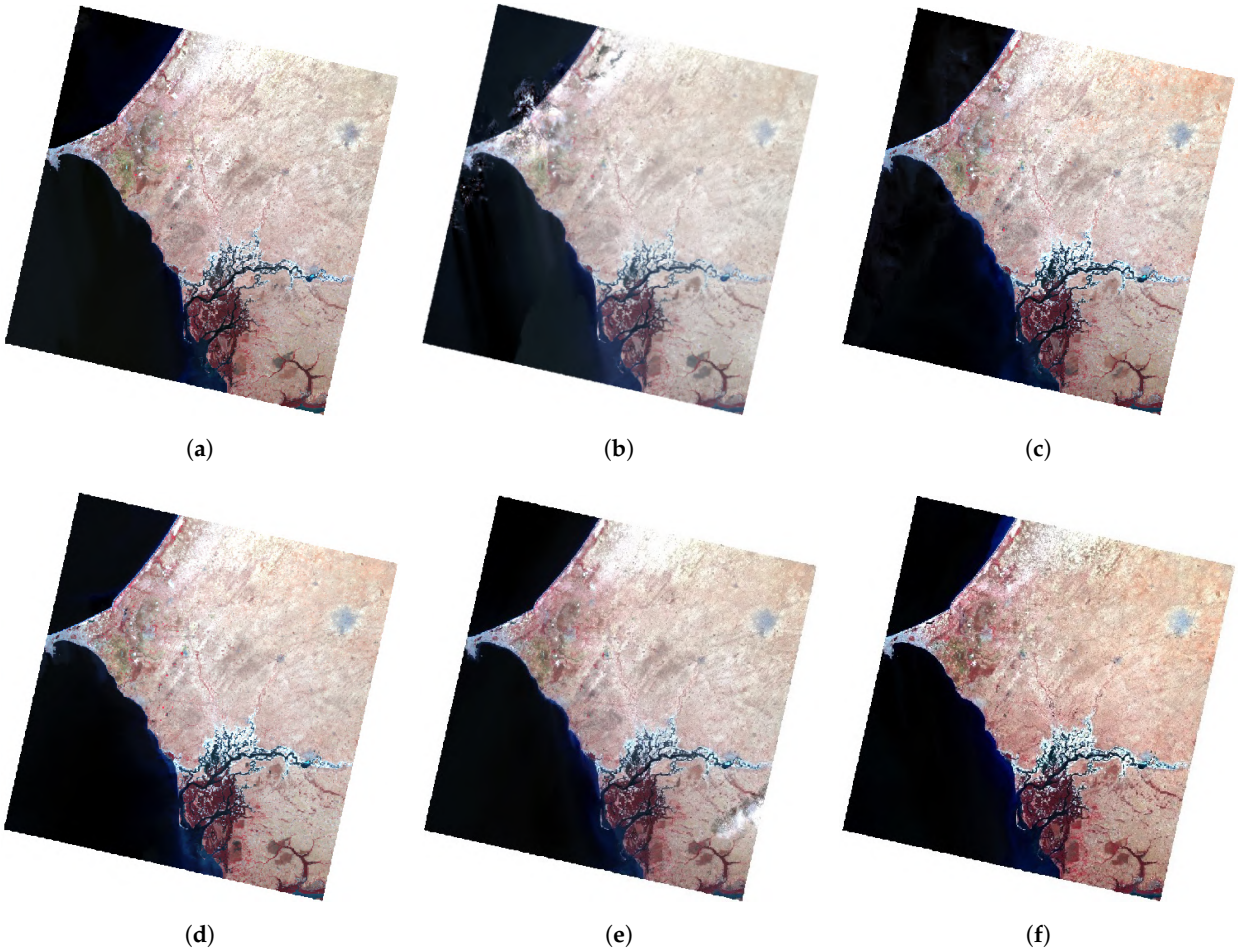

Figure 5. False color composites of the Landsat 8-9 OLI/TIRS images with vegetation colored red, using a combination of spectral bands 5 (Near Infrared (NIR)), 4 (Red), and 3 (Green) of the Landsat OLI sensor covering the study area in the Cape Verde Peninsula region and Saloum River Delta, West Senegal, using February scenes: (**a**) 2015; (**b**) 2018; (**c**) 2020; (**d**) 2021; (**e**) 2022; (**f**) 2023.

The standard requirements for a training dataset in the ML approach that includes the SVM algorithm include a supervised classifier to derive an accurate and precise description of the spectral properties of each land cover type. Therefore, the training data were derived from the previous raster dataset in TIFF format as samples that support vectors through data partition. The target pixels were selected as representative cells located on the edge of the class distribution in feature space. Using GRASS GIS syntax, generating the training pixels from the land cover classification was performed using the following code: 'r.random input=L_2015_clusters seed=100 npoints=1000 raster=training_pixels'. Here, the number of pixels was selected as 1000 for a larger and more representative dataset, and the seed for training the data was set to 100.

Afterwards, the contrasting regions that have distinguished spectral reflectance values (water, savanna, forest, croplands, and urban spaces) were used for identification of similar classes in the evaluated periods. Then, the land cover classes were identified using the SVM algorithm with the modules 'r.learn.train', which trains an SVM model, and 'r.learn.predict', which performs prediction of pixels' association with each of the 10 target land cover classes based on the spectral reflectance of pixels in the images.

3. Results and Discussion

3.1. Interpretation of Key Findings

In this section, the ability of the two algorithms—unsupervised classification by k-means and supervised classification by SVM—to detect land cover changes in the satellite images is evaluated. Specifically, we assessed the dynamics in the distinct habitats of Senegal ranging from arid landscapes with savanna to humid coastal conditions with mangroves. The data for the land cover types in Senegal were visualized in the QGIS software using vector layers in the Environmental Systems Research Institute (ESRI) format; see Figure 6.

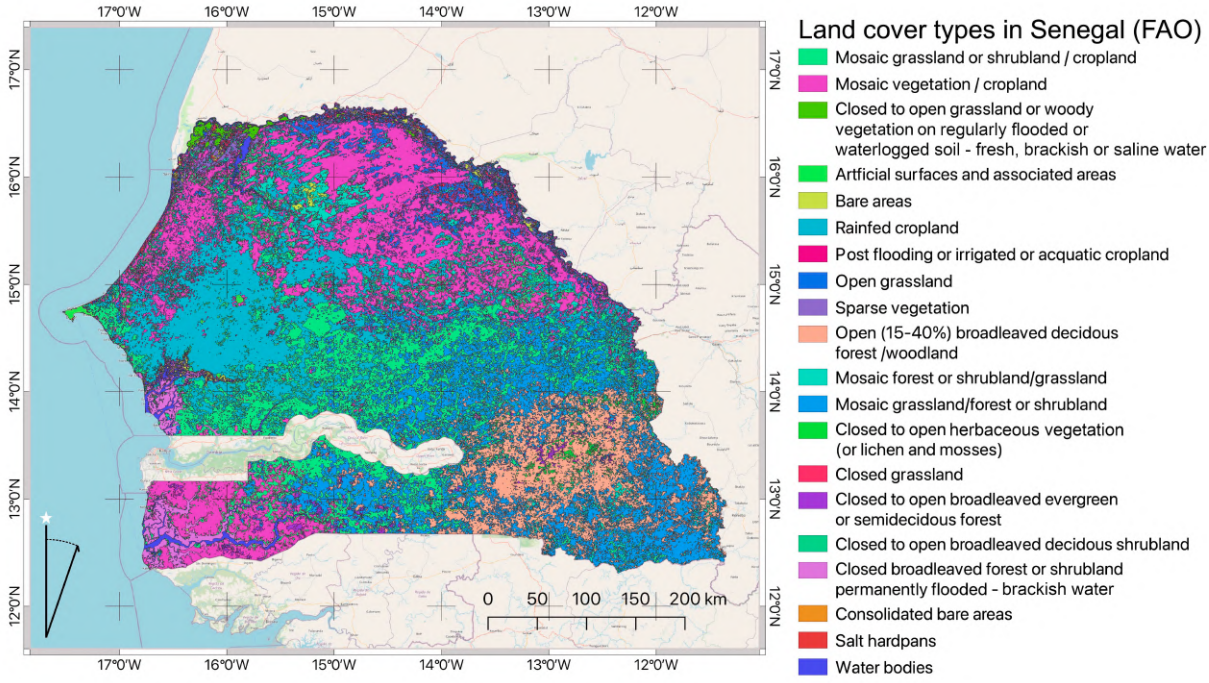

Figure 6. Land cover types in Senegal according to the FAO classification scheme. Software: QGIS v. 3.22. Map source: Author.

According to the Food and Agriculture Organization (FAO)/United Nations Environment Programme (UNEP) classification scheme, the land cover types in Senegal include 10 major classes. These were adopted for the target extent of the ROI through generalization at the country level using the Land Cover Classification System (LCCS) of FAO/UNEP:

1. Mosaic grassland or shrubland/cropland;
2. Mosaic vegetation/cropland;
3. Mangrove wetlands;
4. Rainfed cropland;
5. Consolidated bare areas;
6. Mosaic grassland/forest or shrubland;
7. Closed broadleaved forest or shrubland permanently flooded—brackish water;
8. Salt hardpans;
9. Post-flooding or irrigated or aquatic cropland;
10. Water bodies.

The quantitative estimations of changes in land cover types over the evaluated period (2015 to 2023) are summarized in the tables in Appendix C. They report the computed changes in land cover classes for each processed image. The analysis of these values shows that the northern and southern coastal ecosystems of western Senegal have a relatively small degree of change over the estimated period. In contrast, in the arid north, areas associated with forests and mosaic types of vegetation demonstrate higher magnitudes

of change, suggesting a higher level of instability compared to the estuaries in the south. The classification of the land cover types was adapted to the larger extent of the ROI with details for the coastal area, including mangrove forests. The territory of Senegal comprises eight major biological zones with 11 different forms of land use. Of these, major types include the savanna, cultivated lands, forests, and steppes as the dominating types of land cover in the semi-arid zones [75].

A special focus of coastal Senegalese landscapes is mangrove swampland, a crucial habitat in the west of the country. Mangroves provide a source of natural resources [76] and a habitat for wildlife species [77]. At the same time, diverse factors have strongly correlated with mangrove losses. These include climate-related processes such as changes in temperature and precipitation, flooding, and increased salinization of waters, as well as human-related factors such as increases in intensive urbanization [78] and active agriculture practices [79]. Overall, the analysis of land cover types over the coastal area shows the variability in mangroves (bright cyan in Figure 6). Coastal dynamics are explained by high interannual fluctuations in the delta of the Saloum River: the upper tidal zone is flooded during high tide, while during the drought period, it remains drained, with high evaporation resulting in soil salinization.

3.2. Clustering-Based Classification

The overview of Figure 7, on which are overlaid the 2015–2023 Landsat OLI/TIRS time series and the land cover types for each case, shows the diversity of habitats and the intensity of changes detected in the images classified by the k-means algorithm. The analysis of the classified images based on clustering shows a trend in land cover dynamics of the coastal region of Senegal over Dakar and its surroundings.

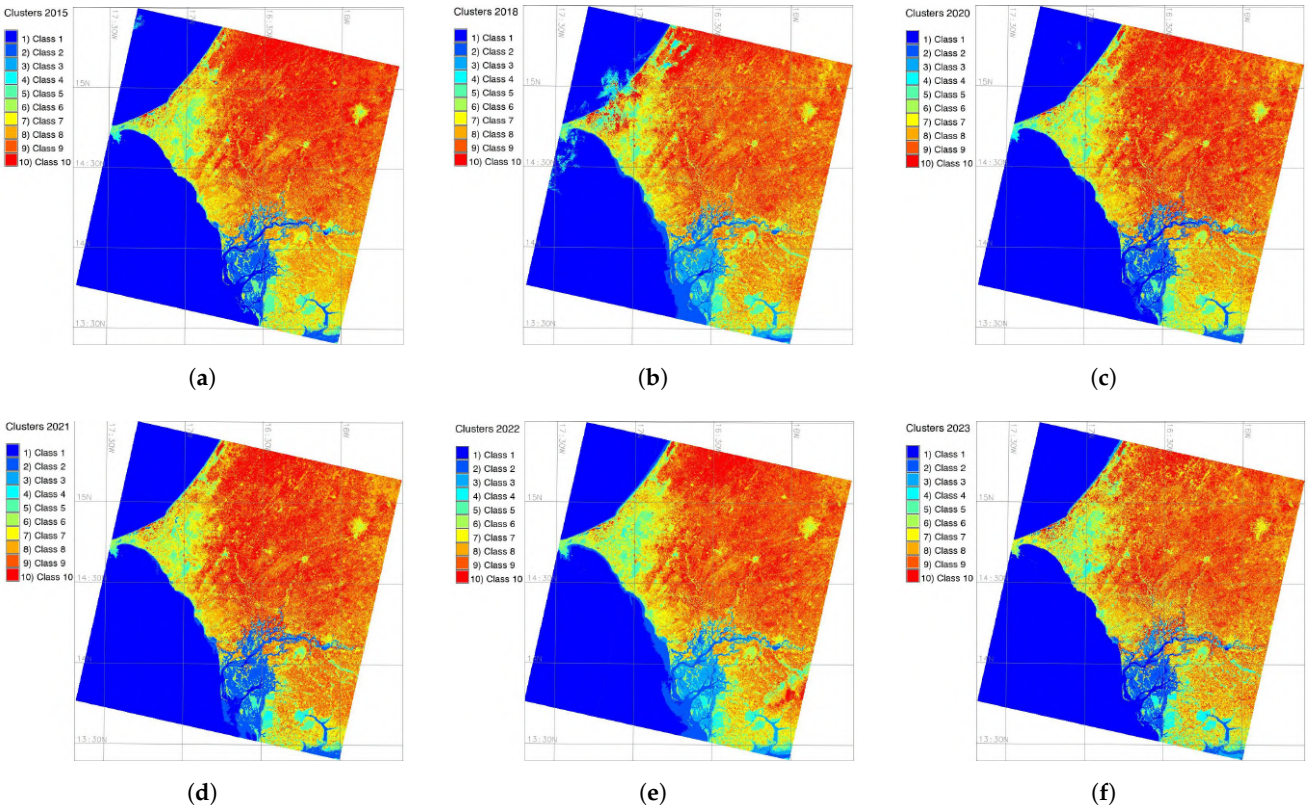

Figure 7. Classification of the Landsat images from 2020 covering the Cape Verde Peninsula region and the Saloum River Delta, West Senegal: (**a**) 2015; (**b**) 2018; (**c**) 2020; (**d**) 2021; (**e**) 2022; (**f**) 2023.

The results demonstrate that the dominating land cover type of Senegal remains savanna (73%), although the areas covered by savanna showed a slight decrease since 2015. In contrast, the landscapes covered by croplands and agricultural areas expanded

to 22%. Furthermore, the decline in the area covered by forests and mangroves is notable. Nevertheless, in general, the dominating land cover types in Senegal remain savannas, woodlands, and forests, covering over 75% of the country, a result aligned with similar studies [24].

The maps of land cover change based on the classified imagery display different spatial patterns. While forest and savanna in the subplots have a significantly higher magnitude of values than the background, this is not the case for the bushland and grasslands, where the difference between the values inside and outside is minimal. The croplands demonstrate moderate changes that indicate the measures taken for sustainable management in Senegal. Overall, landscape heterogeneity can be observed in comparing the processed images. The southern sector of Senegalese vegetation is characterized by the Sudano-Guinean forest savanna and the Guinean forests [80].

The most pronounced variations in land cover types in western Senegal detected on the processed and classified satellite images reflect the relationships and links between changing vegetation and soil characteristics that are subject to climatic factors, moisture level, salinity, and organic matter, as noted earlier [81]. Moreover, the pattern of changes in the agricultural land cover types over time correlate with seasonal fluctuations in the crop–fallow cycle. Agricultural plantations and irrigated lands are distributed in sporadic settlements along the populated and semi-urban areas. Earlier studies also noted [82] that climate variability is the dominant factor that leads to increasing the actual evaporation and, as a result, to land salinization in the basin of the Senegal River.

3.3. Support Vector Machine (SVM)-Based Classification

The SVM-based classification of the dynamics of land cover types in Senegal based on the Landsat OLI/TIRS scenes (2015–2023) resulted in the generation of the thematic maps of land cover types shown in Figure 8, in which the most important classes are identified as follows: the rainfed cropland class is depicted in aquamarine; water areas are shown in blue; mosaic vegetation is colored bright red; and grassland, forest, and shrubland areas are shown in orange. The numerical results obtained for the different images using classification models of GRASS GIS are summarized in Appendix C. Generally, the classification of the Landsat scenes using the SVM algorithm applied to the reflective multispectral bands of the image (channels 1 to 7) provided excellent results for each kernel of the 10 categorized classes.

The aim of the SVM application is to improve the accuracy of recognition of land cover types and to increase the quality of mapping. The feasibility of land cover change analysis depends on the quality of cartographic techniques when processing RS data. Erroneously recognizing trends may arise from the use of land cover regions derived from unadjusted classifiers that exhibit imbalanced misclassification between distinct groups. Therefore, in our work, we used the effective approach of the SVM algorithm proposed by GRASS GIS, which presents a ML approach for image classification. The scripts used for SVM-based image processing are presented in Appendix B.

The detected landscape dynamics evaluated using a time series of the satellite images indicate the cumulative effects of anthropogenic activities and climate change in the semi-arid region of West Africa. This involves such processes as variability of precipitation, increase in temperature, land erosion, and wildfire. These factors control the distribution of croplands, natural vegetation systems, and coastal mangrove colonies in western Senegal. The main triggers for changing types of vegetation and landscape patterns in the Senegalese Sahel include climatic factors and anthropogenic activities, which have resulted in the decline and local extinction of woody species [83].

Among other land cover types, the relics of the Guinean forest are distributed in the northern part of Senegal as a narrow band of landscapes stretching parallel to the Atlantic coast. In the southern and eastern regions off Dakar and around the region of Thiès, there are many species that are abundant in the north of the forest and represented by the scattered trees in the Sudano-Sahelian savanna.

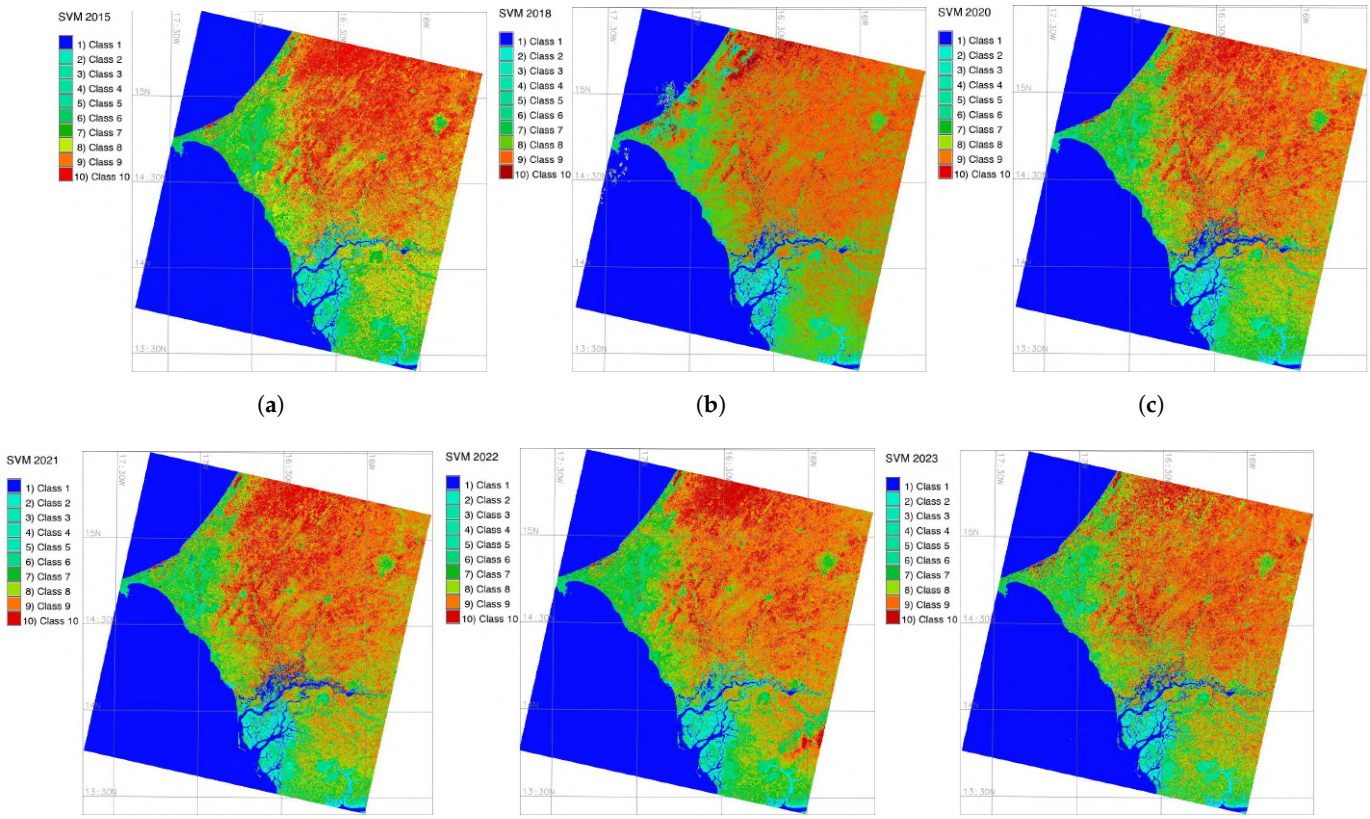

Figure 8. Results of the Support Vector Machine (SVM)-based classification of the Landsat images covering the Cape Verde Peninsula region and Saloum River Delta, West Senegal: (**a**) February 2015; (**b**) February 2018; (**c**) February 2020; (**d**) February 2021; (**e**) February 2022; (**f**) February 2023.

To the east of Dakar, the northern silvopastoral zone of Senegal presents a vast silvopastoral zone characterized around the Ferlo region, which is notable for its extreme aridity, dominated by land cover types of shrubby savanna and steppe vegetation [84]. The enclaves of hygrophilous vegetation surrounding the coastal wetlands are located to the north of Dakar, with mangroves as the dominant land cover type. Additionally, this region includes the occasional groves of the oil palm as spontaneous landscape features of the Guinean forests.

3.4. Accuracy Analysis

Figure 9 shows the results of the accuracy assessment. The correctness of the assignment of pixels to the target classes was evaluated based on the pixel confidence levels with rejection probability values. Using the algorithms embedded in GRASS GIS, six classified Landsat images were evaluated against the probability of the identified pixels being classified into the correct land cover class. In this way, possible misclassification that may arise due to the similar spectral reflectance values in land cover types was assessed. It can be seen that there is a good linear correlation between the contours of the land cover classes and the accuracy of the classification of pixels. The estimation of the values of spectral reflectance indicates a general assignment to a given land cover type. The results are similar for the classified Landsat images processed by means of scripts and correspond to the different land cover types, such as coastal areas, water, savanna, Guinean forests, and agricultural lands.

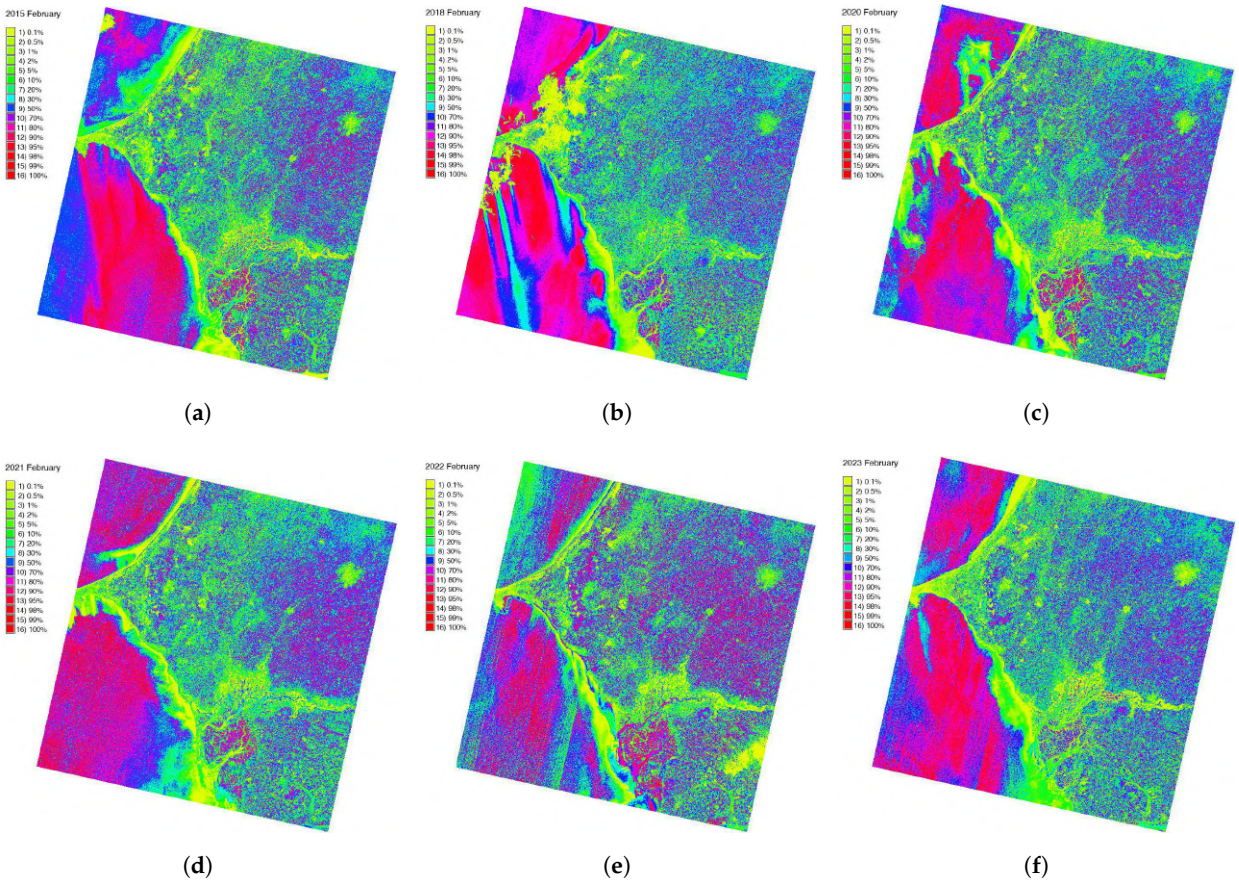

Figure 9. Accuracy evaluated based on the pixel confidence levels with rejection probability values for the Landsat images covering the Cape Verde Peninsula region and Saloum River Delta, West Senegal: (**a**) 2015; (**b**) 2018; (**c**) 2020; (**d**) 2021; (**e**) 2022;(**f**) 2023.

3.5. Implications and Discussion

Land cover types in Senegal present fluctuations in vegetation patterns as a result of long-term landscape evolution in West Africa [85–88]. The cumulative effects of climate, environmental, and anthropogenic factors led to a decrease in mangrove colonies, which decline in high-salinity waters [89]. This is also supported by previous studies that report the retreat of the mangrove in the advance of the tannes [90]. At the same time, the trend in rainfall recovery in West Senegal since the 1990s [65] has resulted in the rehabilitation of mangroves, which restored their colonies accordingly, as also visible on the images. This corresponds with the results of the existing reports on the location and distribution of *Rhizophora mangle* and *Avicennia germinans* mangrove species in western Senegal [91,92]. Earlier works also noted the increase in mangrove trees in the estuaries of Senegal [93]. In addition to the coastal ecosystems, the areas occupied by crop production follow the same trend in changes, possibly due to vegetation removal associated with plot preparation on agricultural land.

Human-induced activities such as agricultural, demographic, and socioeconomic changes have affected the environmental settings and habitats of Senegal. Although the human impacts on the region were negligible for decades due to the relatively low population density of Senegal, recently, a natural increase in the population has accelerated the exploitation of natural and mineral resources. As a result, this has triggered land degradation in the coastal areas. Consequently, select landscapes of Senegal are subject to the deterioration of valuable habitats, fragmentation of patches, and land cover changes. Major human-induced factors in Senegal are related to dynamic agribusiness in terms of agricultural commodities, which increases the areas of irrigated vegetation and croplands [94]. Although such activities are vital for supporting the local population, the environmental

consequences on Senegalese landscapes include changed land cover types. Additionally, land degradation in the savanna landscapes correlates with trends in land cover changes and a significant decrease in woodlands [95].

To summarize, this paper reports the results obtained from experimental investigations into land cover types in Senegal analyzed using a ML approach and the SVM algorithm, compared and evaluated against the traditional unsupervised classification method of k-means clustering. The performance of SVM demonstrated reliable results in image processing, outperforming clustering in terms of accuracy and speed of data processing. To this end, a time series of Landsat scenes was processed using GRASS GIS software. The image processing was designed using a set of modules processed by scripts for automation. Interactive processing and scripts adjusted for each scene provided an effective way to process satellite images in workflow chain. Such automation enabled us to represent complex interactions within the landscapes in a short-term perspective by accurate ML-based mapping using a comparison of the SVM and k-means methods. In this way, this study has presented an advanced data-driven method of image analysis for automatically detecting changes in land cover types in a selected ROI of Senegal.

4. Conclusions

Mapping land cover types, discriminating mangroves, and monitoring savanna ecosystems are essential for proper land management in Senegal. In this study, the potential for employing the SVM algorithm classifier in conjunction with Landsat OLI/TIRS multispectral satellite images was evaluated to map areas of land cover in the environment of Senegal. In an effort to drive research in this field, this paper proposed a series of image classification experiments using the GRASS GIS scripting approach, which served as a means of ranking landscapes. Using processed satellite images, land cover development was evaluated in the condition of the unstable environmental setting of western Senegal, which has been affected by climate change and human activities. The practical aim was to evaluate the variations in land cover types in the western segment of Senegal around the Cape Verde Peninsula and Dakar and its surroundings during 2015–2023. The presented results confirm that RS data can be effectively used to evaluate the variations in landscapes in West Africa.

To evaluate the performance of GRASS GIS in image processing, the multispectral bands of six images were analyzed for matching landscape comparisons for different years, and the classification accuracy is reported as rejection probability for pixels in each Landsat scene. Hence, the advantage of the use of the RS data for environmental monitoring is that they provide an efficient way to map and visualize the remotely located regions that are otherwise difficult to reach, such as West Africa. The analysis of the extent and distribution of the selected landscapes in a series of satellite images and the decrease in minor patches enabled us to detect environmental landscape dynamics in a selected ROI. We also provided remarks on the factors affecting changes in land cover types based on the analysis of the processed images compared to previous case studies in the published literature. The major driving factors include the related environmental climate processes and human activities that resulted in land cover changes in Senegal. Such notes can be used in similar works with a focus on environmental changes, and land cover type changes in Senegal can continue to be investigated.

Author Contributions: Conceptualization, P.L.; methodology, P.L.; software, P.L.; validation, P.L.; formal analysis, P.L.; investigation, P.L.; resources, P.L.; data curation, P.L.; writing—original draft preparation, P.L.; writing—review and editing, P.L.; visualization, P.L.; supervision, P.L.; project administration, P.L.; funding acquisition, P.L. All authors have read and agreed to the published version of the manuscript

Funding: The publication was funded by the Editorial Office of Earth, Multidisciplinary Digital Publishing Institute (MDPI), by providing a discount for the APC of this manuscript and Institutional Open Access Program (IOAP) participating institution University of Salzburg

Data Availability Statement: The author's GitHub repository, with scripts used for image classification and the results of the Support Vector Machine (SVM) ML-based processing of the satellite images, is available online at: https://github.com/paulinelemenkova/Senegal_Scripts (accessed on 14 August 2024).

Acknowledgments: The author thanks the reviewers for reading and reviewing this manuscript.

Conflicts of Interest: The author declares no conflicts of interest.

Abbreviations

The following abbreviations are used in this manuscript:

DCW	Digital Chart of the World
DEM	Digital Elevation Model
DL	Deep Learning
DN	Digital Number
ESRI	Environmental Systems Research Institute
FAO	Food and Agriculture Organization
GEBCO	General Bathymetric Chart of the Oceans
GMT	Generic Mapping Tools
GRASS	Geographic Resources Analysis Support System
LCCS	Land Cover Classification System
GIS	Geographic Information System
GUI	Graphical User Interface
Landsat MSS	Landsat Multispectral Scanner
Landsat TM	Landsat Thematic Mapper
Landsat ETM+	Landsat Enhanced Thematic Mapper Plus
Landsat OLI/TIRS	Landsat Operational Land Imager and Thermal Infrared Sensor
ML	Machine Learning
NDVI	Normalized Difference Vegetation Index
NIR	Near-Infrared
ROI	Region of Interest
RS	Remote Sensing
SRTM	Shuttle Radar Topography Mission
SVC	Support Vector Classification
SVM	Support Vector Machine
TIFF	Tag Image File Format
UNEP	United Nations Environment Programme
USGS	United States Geological Survey
UTM	Universal Transverse Mercator

Appendix A. Metadata of the Landsat 8-9 OLI/TIRS Images

Appendix A.1. Images from 2015, 2018, and 2020

Table A1. Metadata of Landsat OLI/TIRS satellite images of Senegal for the years 2015, 2018, and 2020.

Dataset Attribute	Attribute Value (2015)	Attribute Value (2018)	Attribute Value (2020)
Landsat Scene Identifier	LC82050502015056LGN01	LC82050502018048LGN00	LC82050502020038LGN00
Date Acquired	2015/02/25	2018/02/17	2020/02/07
Collection Category	T1	T1	T1
Collection Number	2	2	2
WRS Path	205	205	205
WRS Row	50	50	50
Target WRS Path	205	205	205
Target WRS Row	50	50	50
Nadir/Off Nadir	NADIR	NADIR	NADIR
Roll Angle	0.000	0.000	0.000
Date Product Generated L2	9 September 2020	2 September 2020	23 August 2020
Date Product Generated L1	9 September 2020	2 September 2020	23 August 2020
Start Time	25 February 2015 11:27:00.070962	17 February 2018 11:26:59.893161	7 February 2020 11:27:15.666422

Table A1. *Cont.*

Data Set Attribute	Attribute Value (2015)	Attribute Value (2018)	Attribute Value (2020)
Stop Time	25 February 2015 11:27:31.840958	17 February 2018 11:27:31.663159	7 February 2020 11:27:47.436421
Station Identifier	LGN	LGN	LGN
Day/Night Indicator	DAY	DAY	DAY
Land Cloud Cover	0.04	2.05	0.20
Scene Cloud Cover L1	0.05	2.22	2.80
Ground Control Points Model	771	726	742
Ground Control Points Version	5	5	5
Geometric RMSE Model	3.594	4.364	4.488
Geometric RMSE Model X	2.608	3.059	3.131
Geometric RMSE Model Y	2.472	3.113	3.215
Processing Software Version	LPGS_15.3.1c	LPGS_15.3.1c	LPGS_15.3.1c
Sun Elevation L0RA	53.48558579	51.49601301	49.10812112
Sun Azimuth L0RA	128.54617537	131.78990105	135.75967932
TIRS SSM Model	FINAL	FINAL	FINAL
Data Type L2	OLI_TIRS_L2SP	OLI_TIRS_L2SP	OLI_TIRS_L2SP
Sensor Identifier	OLI_TIRS	OLI_TIRS	OLI_TIRS
Satellite	8	8	8
Product Map Projection L1	UTM	UTM	UTM
UTM Zone	28	28	28
Datum	WGS84	WGS84	WGS84
Ellipsoid	WGS84	WGS84	WGS84
Scene Center Lat DMS	14°27′25.70″ N	14°27′24.62″ N	14°27′24.37″ N
Scene Center Long DMS	16°39′49.72″ W	16°38′25.62″ W	16°38′00.28″ W
Corner Upper Left Lat DMS	15°29′56.47″ N	15°29′57.59″ N	15°29′57.84″ N
Corner Upper Left Long DMS	17°44′21.55″ W	17°42′51.05″ W	17°42′30.92″ W
Corner Upper Right Lat DMS	15°30′54.65″ N	15°30′54.86″ N	15°30′54.94″ N
Corner Upper Right Long DMS	15°36′21.85″ W	15°35′01.32″ W	15°34′31.12″ W
Corner Lower Left Lat DMS	13°23′18.24″ N	13°23′19.18″ N	13°23′19.39″ N
Corner Lower Left Long DMS	17°42′48.92″ W	17°41′19.25″ W	17°40′59.34″ W
Corner Lower Right Lat DMS	13°24′08.14″ N	13°24′08.32″ N	13°24′08.39″ N
Corner Lower Right Long DMS	15°36′01.33″ W	15°34′41.56″ W	15°34′11.60″ W
Scene Center Latitude	14.45714	14.45684	14.45677
Scene Center Longitude	−16.66381	−16.64045	−16.63341
Corner Upper Left Latitude	15.49902	15.49933	15.49940
Corner Upper Left Longitude	−17.73932	−17.71418	−17.70859
Corner Upper Right Latitude	15.51518	15.51524	15.51526
Corner Upper Right Longitude	−15.60607	−15.58370	−15.57531
Corner Lower Left Latitude	13.38840	13.38866	13.38872
Corner Lower Left Longitude	−17.71359	−17.68868	−17.68315
Corner Lower Right Latitude	13.40226	13.40231	13.40233
Corner Lower Right Longitude	−15.60037	−15.57821	−15.56989

Appendix A.2. Images from 2021, 2022, and 2023

Table A2. Metadata of Landsat OLI/TIRS satellite images of Senegal for the years 2021, 2022, and 2023.

Data Set Attribute	Attribute Value (2021)	Attribute Value (2022)	Attribute Value (2023)
Landsat Scene Identifier	LC82050502021056LGN00	LC92050502022051LGN01	LC92050502023022LGN01
Date Acquired	25 February 2021	20 February 2022	22 January 2023
Collection Category	T1	T1	T1
Collection Number	2	2	2
WRS Path	205	205	205
WRS Row	50	50	50
Target WRS Path	205	205	205
Target WRS Row	50	50	50
Nadir/Off Nadir	NADIR	NADIR	NADIR
Roll Angle	0.000	0.000	0.000
Date Product Generated L2	4 March 2021	27 April 2023	13 March 2023
Date Product Generated L1	4 March 2021	27 April 2023	13 March 2023
Start Time	25 February 2021 11:27:13.15558	20 February 2022 11:27:20	22 January 2023 11:27:31
Stop Time	25 February 2021 11:27:44.925579	20 February 2022 11:27:52	22 January 2023 11:28:03
Station Identifier	LGN	LGN	LGN
Day/Night Indicator	DAY	DAY	DAY
Land Cloud Cover	0.09	0.54	0.21
Scene Cloud Cover L1	0.06	0.37	0.15
Ground Control Points Model	734	706	709
Ground Control Points Version	5	5	5
Geometric RMSE Model	5.012	5.380	5.233
Geometric RMSE Model X	3.552	3.866	3.747
Geometric RMSE Model Y	3.536	3.741	3.653

Table A2. *Cont.*

Data Set Attribute	Attribute Value (2021)	Attribute Value (2022)	Attribute Value (2023)
Processing Software Version	LPGS_15.4.0	LPGS_16.2.0	LPGS_16.2.0
Sun Elevation L0RA	53.68773361	52.31756922	46.40104898
Sun Azimuth L0RA	128.38743700	130.64790443	140.80741499
TIRS SSM Model	FINAL	N/A	N/A
Data Type L2	OLI_TIRS_L2SP	OLI_TIRS_L2SP	OLI_TIRS_L2SP
Sensor Identifier	OLI_TIRS	OLI_TIRS	OLI_TIRS
Satellite	8	9	9
Product Map Projection L1	UTM	UTM	UTM
UTM Zone	28	28	28
Datum	WGS84	WGS84	WGS84
Ellipsoid	WGS84	WGS84	WGS84
Scene Center Lat DMS	14°27′25.24″N	14°27′25.16″N	14°27′24.19″N
Scene Center Long DMS	16°38′36.71″W	16°39′35.46″W	16°38′55.97″W
Corner Upper Left Lat DMS	15°29′57.37″N	15°29′46.86″N	15°29′47.36″N
Corner Upper Left Long DMS	17°43′11.14″W	17°44′11.36″W	17°43′31.15″W
Corner Upper Right Lat DMS	15°30′54.83″N	15°30′44.93″N	15°30′45″N
Corner Upper Right Long DMS	15°35′11.36″W	15°36′01.69″W	15°35′31.49″W
Corner Lower Left Lat DMS	13°23′18.96″N	13°23′18.35″N	13°23′18.74″N
Corner Lower Left Long DMS	17°41′39.19″W	17°42′38.95″W	17°41′59.10″W
Corner Lower Right Lat DMS	13°24′08.32″N	13°24′08.21″N	13°24′08.24″N
Corner Lower Right Long DMS	15°34′51.53″W	15°35′41.39″W	15°35′11.47″W
Scene Center Latitude	14.45701	14.45699	14.45672
Scene Center Longitude	−16.64353	−16.65985	−16.64888
Corner Upper Left Latitude	15.49927	15.49635	15.49649
Corner Upper Left Longitude	−17.71976	−17.73649	−17.72532
Corner Upper Right Latitude	15.51523	15.51248	15.51250
Corner Upper Right Longitude	−15.58649	−15.60047	−15.59208
Corner Lower Left Latitude	13.38860	13.38843	13.38854
Corner Lower Left Longitude	−17.69422	−17.71082	−17.69975
Corner Lower Right Latitude	13.40231	13.40228	13.40229
Corner Lower Right Longitude	−15.58098	−15.59483	−15.58652

Appendix B. Programming Scripts

Appendix B.1. GMT Script

Listing A1. GMT code for topographic mapping of the Senegal region based on the GEBCO/SRTM dataset.

```
exec bash
# Extract a subset of ETOPO1m for the study area
gmt grdcut ETOPO1_Ice_g_gmt4.grd -R-18/-11/12/17 -Gsn1_relief.nc
gmt grdcut GEBCO_2019.nc -R-18/-11/12/17 -Gsn_relief.nc
gdalinfo -stats sn1_relief.nc
gmt makecpt -Cillumination -V -T-5000/500 -Ic > pauline.cpt
# create mask of vector layer from the DCW of country's polygon
gmt pscoast -R-18/-11/12/17 -JM6.5i -Dh -M -ESN > Senegal.txt
ps=Topo_SN.ps
# Make background transparent image
gmt grdimage sn_relief.nc -Cpauline.cpt -R-18/-11/12/17 -JM6.5i -I+a15+ne0.75 -t40 -Xc -
    P -K > $ps
.5i
# Add isolines
gmt grdcontour sn1_relief.nc -R -J -C250 -A250+f7p,26,darkbrown -Wthinner,darkbrown -O -
    K >> $ps
# Add coastlines, borders, rivers
gmt pscoast -R -J \
    -Ia/thinner,blue -Na -N1/thicker,tomato -W0.1p -Df -O -K >> $ps
gmt pscoast -R -J -Ia/thinner,blue -Na -Sroyalblue1 -W2/thin,blue,0.1p -Df -O -K >> $ps
gmt psclip -R-18/-11/12/17 -JM6.5i Senegal.txt -O -K >> $ps
gmt grdimage sn_relief.nc -Cpauline.cpt -R-18/-11/12/17 -JM6.5i -I+a15+ne0.75 -Xc -P -O
    -K >> $ps
# Add isolines
gmt grdcontour sn1_relief.nc -R -J -C100 -A250+f7p,26,darkbrown -Wthinnest,darkbrown -O
    -K >> $ps
# Add coastlines, borders, rivers
gmt pscoast -R -J \
    -Ia/thinner,blue -Na -N1/thicker,tomato -W0.1p -Df -O -K >> $ps
gmt pscoast -R -J -Ia/thinner,blue -Na -Sroyalblue1 -W2/thin,blue,0.1p -Df -O -K >> $ps
gmt psclip -C -O -K >> $ps
gmt psscale -Dg-18/11.5+w16.5c/0.15i+h+o0.3/0i+ml+e -R -J -Cpauline.cpt \
    -Bg1000f50a500+l''Colormap: 'illumination', ESRI cartographic and geospatial
    gradient, continuous, 126 segments, C=RGB'' \
    -I0.2 -By+l''m'' -O -K >> $ps
# Add grid
gmt psbasemap -R -J \
```

```
    --MAP_FRAME_AXES=WEsN  --FORMAT_GEO_MAP=ddd:mm:ssF \
        -Bpxg4f1a2 -Bpyg4f1a1 -Bsxg2 -Bsyg1 \
    -B+t''Topographic map of Senegal'' -O -K >> $ps
# Add scalebar, directional rose
gmt psbasemap -R -J \
    -Lx14.0c/-2.5c+c10+w200k+l''Mercator projection. Scale (km)''+f \
    -UBL/0p/-70p -O -K >> $ps
gmt psxy -R -J -Sj1c -W1.7p,red3 -O -K << EOF >> $ps
-16.68 14.46 -13 4.0 4.0
EOF
# Texts
gmt pstext -R -J -N -O -K \
-F+f11p,21,darkred+jLB >> $ps << EOF
-13.60 13.60 Tambacounda
EOF
gmt psxy -R -J -Sc -W0.5p -Gyellow -O -K << EOF >> $ps
-13.67 13.77 0.20c
EOF
# repeated likewise for all the text annotations using coordinates
gmt psbasemap -R -J -O -K -DjTL+w3.2c+o-0.2c/-0.2c+stmp >> $ps
read x0 y0 w h < tmp
gmt pscoast --MAP_GRID_PEN_PRIMARY=thinnest,lightgray --MAP_FRAME_PEN=thick,white -Rg -
    JG-1.0/8.0N/$w -Da -Glightgoldenrod1 -A5000 -Bga -Wfaint -ESN+gred -Sroyalblue1 -O
    -K -X$x0 -Y$y0 >> $ps
gmt psxy -R -J -O -K -T  -X-${x0} -Y-${y0} >> $ps
gmt logo -Dx7.0/-3.1+o0.1i/0.1i+w2c -O -K >> $ps
gmt pstext -R0/10/0/15 -JX10/10 -X0.5c -Y5.5c -N -O \
    -F+f10p,0,black+jLB >> $ps << EOF
2.5 11.0 Digital elevation data: SRTM/GEBCO, 15 arc sec resolution grid
EOF
gmt psconvert Topo_SN.ps -A0.5c -E720 -Tj -Z
```

Appendix B.2. R Script

Listing A2. R code for modeling the flowchart of the methodological process.

```
DiagrammeR::grViz('
digraph Polina_diagram {
 # graph statement
  graph [layout = dot, rankdir = TB,   # layout top-to-bottom fontsize = 12]
  node [shape = circle,
        fixedsize = true, width = 2.0]
  subgraph cluster2 {
  node [fillcolor = Bisque, shape = egg, fontname = Helvetica, fontcolor = darkslategray
     , shape = rectangle, fixedsize = true, width = 4.0, color = darkslategray,
     linewidth = 2.0]
  A66 [label = 'Landsat 9 OL/TIRS image \nJanuary 2023 \nLC92050502023022LGN01', shape =
      rectangle, fontsize = 22, height = 1.5]
  A55 [label = 'Landsat 9 OL/TIRS image \nFebruary 2022 \nLC92050502022051LGN01', shape
     = rectangle, fontsize = 22, height = 1.5]
  A44 [label = 'Landsat 8 OL/TIRS image \nFebruary 2021 \nLC82050502021056LGN00', shape
     = rectangle, fontsize = 22, height = 1.5]
  A33 [label = 'Landsat 8 OL/TIRS image \nFebruary 2020 \nLC82050502020038LGN00', shape
     = rectangle, fontsize = 22, height = 1.5]
  A22 [label = 'Landsat 8 OL/TIRS image \nFebruary 2018 \nLC82050502018048LGN00', shape
     = rectangle, fontsize = 22, height = 1.5]
  A11 [label = 'Landsat 8 OL/TIRS image \nFebruary 2015 \nLC82050502015056LGN01', shape
     = rectangle, fontsize = 22, height = 1.5]
  }

  A11 -> A22 [fontcolor = red, color = red, style = dashed]
  A33 -> A44 [fontcolor = red, color = red, style = dashed]
  A55 -> A66 [fontcolor = red, color = red, style = dashed]


  E [label = 'Data import \npreprocessing \nGDAL', fontcolor = darkgreen, shape = egg,
     fontsize = 24, height = 2.0, width = 2.3 ]
  A44 -> E [fontcolor = darkgreen,color = darkgreen, style = dashed]

  F [label = 'Data processing \nGRASS GIS', fontcolor = black, height = 1.5, width =
     2.5, shape = tab, fontsize = 24]
  subgraph cluster6 {
  node [fillcolor = Bisque, shape = egg, fontname = Helvetica, fontcolor = darkslategray
     , shape = rectangle, fixedsize = true, width = 2.5, color = darkslategray]
  F6 [label = '6. Data import \nd.out.file module', fontcolor = black, shape = rectangle
     , width = 3.5, height = 1.3, fontsize = 22]
  F5 [label = '5. Visualization \nd.rast, d.legend \nr.colors', fontcolor = black, shape
      = rectangle, width = 3.5, height = 1.3, fontsize = 22]
```

```
  F4 [label = '4. Accuracy \nassessment', fontcolor = black, shape = rectangle, width =
    2.5, height = 1.3, fontsize = 22]
  F3 [label = '3. Classification\n k-means \ni.maxlik module', fontcolor = black, shape
    = rectangle, width = 2.5, height = 1.3, fontsize = 22]
  F2 [label = '2. Clustering \ni.cluster module', fontcolor = black, shape = rectangle,
    width = 2.5, height = 1.3, fontsize = 22]
  F1 [label = '1. Grouping \ni.group module', fontcolor = black, shape = rectangle,
    width = 2.5, height = 1.3, fontsize = 22]
  }

  F1 -> F2 [fontcolor = red, color = red, style = dashed]
  F3 -> F4 [fontcolor = red, color = red, style = dashed]
  F5 -> F6 [fontcolor = red, color = red, style = dashed]
  E -> F [fontcolor = red, color = red, fontsize = 20, style = twodash]
  F -> {F3} [fontcolor = red, color = red, style = dashed]
}
')
```

Appendix B.3. GRASS GIS Script for Unsupervised Image Classification

Listing A3. GRASS GIS code for classification of the Senegal coastal region based on the segmented raster image Landsat 9 OLI/TIRS.

```
g.list rast
# importing the image subset with 7 Landsat bands and display the raster map
r.import input=/Users/polinalemenkova/grassdata/Senegal/
    LC08_L2SP_205050_20150225_20200909_02_T1_SR_B1.TIF output=L8_2015f_01 resample=
    bilinear extent=region resolution=region --overwrite
r.import input=/Users/polinalemenkova/grassdata/Senegal/
    LC08_L2SP_205050_20150225_20200909_02_T1_SR_B2.TIF output=L8_2015f_02 extent=region
     resolution=region
r.import input=/Users/polinalemenkova/grassdata/Senegal/
    LC08_L2SP_205050_20150225_20200909_02_T1_SR_B3.TIF output=L8_2015f_03 extent=region
     resolution=region
r.import input=/Users/polinalemenkova/grassdata/Senegal/
    LC08_L2SP_205050_20150225_20200909_02_T1_SR_B4.TIF output=L8_2015f_04 extent=region
     resolution=region
r.import input=/Users/polinalemenkova/grassdata/Senegal/
    LC08_L2SP_205050_20150225_20200909_02_T1_SR_B5.TIF output=L8_2015f_05 extent=region
     resolution=region
r.import input=/Users/polinalemenkova/grassdata/Senegal/
    LC08_L2SP_205050_20150225_20200909_02_T1_SR_B6.TIF output=L8_2015f_06 extent=region
     resolution=region
r.import input=/Users/polinalemenkova/grassdata/Senegal/
    LC08_L2SP_205050_20150225_20200909_02_T1_SR_B7.TIF output=L8_2015f_07 extent=region
     resolution=region
g.list rast
# Set computational region to match the scene
g.region raster=L8_2015f_01 -p
# store VIZ, NIR, MIR into group/subgroup (leaving out TIR)
i.group group=L8_2015f subgroup=res_30m \
  input=L8_2015f_01,L8_2015f_02,L8_2015f_03,L8_2015f_04,L8_2015f_05,L8_2015f_06,
    L8_2015f_07
# Clustering: generating signature file and report using k-means clustering algorithm
i.cluster group=L8_2015f subgroup=res_30m \
  signaturefile=cluster_L8_2015f \
  classes=10 reportfile=rep_clust_L8_2015f.txt --overwrite
# Classification by i.maxlik module
i.maxlik group=L8_2015f subgroup=res_30m \
  signaturefile=cluster_L8_2015f \
  output=L8_2015f_cluster_classes reject=L8_2015f_cluster_reject --overwrite
# Mapping
d.mon wx0
g.region raster=L8_2015f_cluster_classes -p
r.colors L8_2015f_cluster_classes color=roygbiv -e
# d.rast.leg L8_2014_cluster_classes
d.rast L8_2015f_cluster_classes
d.legend raster=L8_2015f_cluster_classes title=''2015 February'' title_fontsize=14 font=
    ''Helvetica'' fontsize=12 bgcolor=white border_color=white
d.out.file output=Senegal_2015f format=jpg --overwrite
d.mon wx1
g.region raster=L8_2015f_cluster_classes -p
r.colors L8_2015f_cluster_reject color=rainbow -e
d.rast L8_2015f_cluster_reject
d.legend raster=L8_2015f_cluster_reject title=''2015 February'' title_fontsize=14 font='
    'Helvetica'' fontsize=12 bgcolor=white border_color=white
d.out.file output=Senegal_2015f_reject format=jpg --overwrite
```

Appendix B.4. GRASS GIS Script for Supervised Image Classification

Listing A4. GRASS GIS code for machine learning (ML)-based supervised classification of Senegal based on the Support Vector Machine (SVM) algorithm.

```
# train a SVC model using r.learn.train
r.learn.train group=L_2023 training_map=training_pixels \
    model_name=SVC n_estimators=500 save_model=svc_model.gz --overwrite
# perform prediction using r.learn.predict
r.learn.predict group=L_2023 load_model=svc_model.gz \
output=svc_classification --overwrite
# display
r.colors svc_classification color=roygbiv -e
d.mon wx0
d.rast svc_classification
d.grid -g size=00:30:00 color=grey width=0.1 fontsize=16 text_color=grey
d.legend raster=svc_classification title=''SVM 2023'' title_fontsize=19 \
  font=''Helvetica'' fontsize=17 bgcolor=white border_color=white
d.out.file output=SVM_2023 format=jpg --overwrite
```

Appendix C. Quantitative Estimations of Land Cover Types in the Coastal Region of Senegal Based on the Processed Landsat 8-9 OLI/TIRS Images over the Evaluated Period (2015 to 2023)

Appendix C.1. Results of the processing of the Landsat 8 OLI/TIRS Image on February 2015

```
Location: Senegal
Mapset:   PERMANENT
Group:    L8_2015f
Subgroup: res_30m
 L8_2015f_01@PERMANENT
 L8_2015f_02@PERMANENT
 L8_2015f_03@PERMANENT
 L8_2015f_04@PERMANENT
 L8_2015f_05@PERMANENT
 L8_2015f_06@PERMANENT
 L8_2015f_07@PERMANENT
Result signature file: cluster_L8_2015f

Region
  North:   1715415.00  East:    435015.00
  South:   1481685.00  West:    206085.00
  Res:          30.00  Res:         30.00
  Rows:          7791  Cols:         7631  Cells: 59453121
Mask: no

Cluster parameters
  Nombre de classes initiales:  10
 Minimum class size:           17
 Minimum class separation:     0.000000
 Percent convergence:          98.000000
 Maximum number of iterations: 30

 Row sampling interval:        77
 Col sampling interval:        76

Sample size: 6923 points

means and standard deviations for 7 bands

moyennes 9313.63 9913.36 11418.5 12779 15559.1 18683.2 17049.6
écart-type 1408.81 1655.33 2620.26 4080.9 6172.67 8792.36 7774.72

initial means for each band

classe 1    7904.83 8258.03 8798.21 8698.08 9386.46 9890.85 9274.9
classe 2    8217.9 8625.88 9380.49 9604.95 10758.2 11844.7 11002.6
classe 3    8530.97 8993.73 9962.77 10511.8 12129.9 13798.6 12730.3
classe 4    8844.03 9361.58 10545 11418.7 13501.6 15752.4 14458
classe 5    9157.1 9729.43 11127.3 12325.5 14873.3 17706.3 16185.8
classe 6    9470.17 10097.3 11709.6 13232.4 16245 19660.1 17913.5
classe 7    9783.24 10465.1 12291.9 14139.3 17616.7 21614 19641.2
classe 8    10096.3 10833 12874.2 15046.1 18988.4 23567.9 21368.9
classe 9    10409.4 11200.8 13456.4 15953 20360.1 25521.7 23096.6
classe 10   10722.4 11568.7 14038.7 16859.9 21731.8 27475.6 24824.3

class means/stddev for each band
```

```
class 1 (2503)
moyennes 7708.27 7971.29 8281.61 7838.63 7724.56 7842.02 7776.85
écart-type 614.836 518.68 555.632 565.1 556.362 236.765 141.089

class 2 (174)
moyennes 8368.75 8750.26 9831.58 9975.27 13720.3 10955.7 9432.93
écart-type 376.061 402.119 588.14 812.133 1208.55 495.643 348.885

class 3 (41)
moyennes 8950.56 9432.93 10755.2 11252.4 14627.3 12748.4 10559.9
écart-type 842.571 891.022 1064.14 1331.77 1254.33 890.258 651.371

class 4 (26)
moyennes 9312.5 9943.73 11357.9 12152.8 15320.6 15316.1 12905.9
écart-type 1334.09 1698.16 2286.65 2493.63 930.095 1614.89 1416.64

class 5 (97)
moyennes 9063.18 9615.93 10987.1 12135.6 16577.5 18103.9 14902.9
écart-type 660.968 663.225 782.596 885.988 1296.56 1089.48 1060.51

class 6 (190)
moyennes 9312.92 9975.98 11545 13060.4 17391.5 20272.1 17042.2
écart-type 605.69 613.508 738.417 788.717 1013.67 909.448 960.596

class 7 (398)
moyennes 9686.85 10409.6 12166.7 14010.4 18333.7 22099.6 18938.7
écart-type 577.552 601.118 740.347 817.552 887.638 924.991 1002.24

class 8 (748)
moyennes 9968.69 10749.5 12677.7 14839.1 19219 24041.5 20993.1
écart-type 384.465 399.768 541.802 640.277 811.262 764.889 1038.03

class 9 (1023)
moyennes 10295.7 11120.8 13318.6 15784.4 20276.4 25806.6 23111.7
écart-type 326.204 350.963 499.745 613.788 743.646 678.212 995.761

class 10 (1723)
moyennes 10810.3 11678.3 14315 17326.7 21862 27917.3 25880.4
écart-type 477.098 531.086 761.098 998.069 966.941 946.319 1281.54

Distribution des classes
       2503        174         41         26         97
        190        398        748       1023       1723

######## iteration 1 ###########
10 classes, 94.03% points stable
Distribution des classes
       2480        192         47         30        100
        200        397        752       1241       1484

######## iteration 2 ###########
10 classes, 95.96% points stable
Distribution des classes
       2478        190         51         29        109
        209        397        815       1305       1340

######## iteration 3 ###########
10 classes, 96.23% points stable
Distribution des classes
       2478        184         60         25        116
        217        421        859       1334       1229

######## iteration 4 ###########
10 classes, 96.68% points stable
Distribution des classes
       2479        180         64         24        119
        232        450        880       1355       1140

######## iteration 5 ###########
10 classes, 97.21% points stable
Distribution des classes
       2480        179         64         25        122
        241        491        891       1346       1084

######## iteration 6 ###########
10 classes, 97.18% points stable
Distribution des classes
       2480        179         65         24        127
        250        524        903       1356       1015
```

```
######## iteration 7 ###########
10 classes, 97.75% points stable
Distribution des classes
       2480        179         65         23        134
        265        539        919       1344        975

######## iteration 8 ###########
10 classes, 97.66% points stable
Distribution des classes
       2480        179         65         23        138
        285        556        933       1327        937

######## iteration 9 ###########
10 classes, 97.86% points stable
Distribution des classes
       2480        179         65         23        142
        311        566        941       1305        911

######## iteration 10 ###########
10 classes, 98.02% points stable
Distribution des classes
       2480        179         65         24        146
        332        579        946       1284        888

########## final results #############
10 classes (convergence=98.0%)

class separability matrix

        1     2     3     4     5     6     7     8     9    10

  1     0
  2   2.6     0
  3   2.9   0.9     0
  4   3.5   1.7   1.0     0
  5   5.8   2.7   1.5   1.0     0
  6   7.8   4.2   2.6   1.2   1.1     0
  7   9.8   5.4   3.4   1.6   1.9   0.8     0
  8  12.5   6.9   4.3   2.2   2.8   1.6   0.8     0
  9  15.0   8.3   5.3   2.7   3.8   2.6   1.8   1.0     0
 10  13.9   8.4   5.7   3.1   4.3   3.2   2.5   1.9   1.1     0

class means/stddev for each band

class 1 (2480)
moyennes 7702.51 7964.65 8269.03 7821.72 7687.6 7827.04 7769.4
écart-type 612.7 513.618 538.446 535.084 396.623 175.906 116.846

class 2 (179)
moyennes 8297.44 8655.15 9673.68 9747.75 13631.1 10728.5 9287.23
écart-type 374.25 372.167 496.471 647.696 1391.23 696.653 421.041

class 3 (65)
moyennes 8954.78 9466.29 10844.6 11399.3 13997.9 12546.1 10492
écart-type 654.232 681.113 820.521 1001.57 1421.5 1222.53 836.924

class 4 (24)
moyennes 10531.6 11332.8 13190.9 14415.4 16089.6 15780.6 13457.2
écart-type 1243.88 1529.2 2002.57 2126.12 1348.97 1895.08 1678.55

class 5 (146)
moyennes 8898.16 9461 10810.7 12009.3 16763 18658.5 15324.3
écart-type 404.72 353.277 409.337 649.647 1382.33 1197.85 1087.53

class 6 (332)
moyennes 9503.49 10204.1 11885.1 13566.5 17903.4 21153.7 17968.3
écart-type 579.936 595.056 729.293 799.238 987.119 961.223 928.767

class 7 (579)
moyennes 9874.77 10634.7 12493 14531.4 18863.9 23223.6 20046.3
écart-type 497.731 523.55 685.055 776.898 898.427 846.63 901.884

class 8 (946)
moyennes 10145.7 10950.4 13011 15340 19793.5 25070.2 22208.9
écart-type 318.816 345.68 499.136 637.58 857.969 687.293 964.907

class 9 (1284)
moyennes 10479 11319.6 13710.5 16414.9 20943.1 26902 24529.5
écart-type 308.917 338.535 462.98 589.57 662.867 668.832 869.355

class 10 (888)
```

```
moyennes 11071.3 11960.8 14774.2 17995.2 22506.2 28565.2 26783.6
écart-type 469.146 531.252 724.073 878.44 835.179 791.24 1013.62
#################### CLASSES ####################

10 classes, 98.02% points stable

######## CLUSTER END (Fri Jul 28 16:58:35 2023) ########
```

Appendix C.2. Results of the processing of the Landsat 8 OLI/TIRS Image on February 2018

```
Location: Senegal
Mapset:   PERMANENT
Group:    L8_2018f
Subgroup: res_30m
 L8_2018f_01@PERMANENT
 L8_2018f_02@PERMANENT
 L8_2018f_03@PERMANENT
 L8_2018f_04@PERMANENT
 L8_2018f_05@PERMANENT
 L8_2018f_06@PERMANENT
 L8_2018f_07@PERMANENT
Result signature file: cluster_L8_2018f

Region
  North:   1715145.00  East:    435015.00
  South:   1481685.00  West:    209355.00
  Res:          30.00  Res:         30.00
  Rows:          7782  Cols:         7522  Cells: 58536204
Mask: no

Cluster parameters
  Nombre de classes initiales:  10
 Minimum class size:           17
 Minimum class separation:     0.000000
 Percent convergence:          98.000000
 Maximum number of iterations: 30

 Row sampling interval:        77
 Col sampling interval:        75

Sample size: 7009 points

means and standard deviations for 7 bands

moyennes 8857.44 9492.87 10953.4 12229.7 15198.4 18028.8 15884.1
écart-type 1621.26 1786.57 2482.6 3723.54 5842.65 8100.61 6660.89

initial means for each band

classe 1    7236.18 7706.31 8470.82 8506.2 9355.74 9928.24 9223.22
classe 2    7596.46 8103.32 9022.51 9333.66 10654.1 11728.4 10703.4
classe 3    7956.74 8500.34 9574.2 10161.1 11952.5 13528.5 12183.6
classe 4    8317.02 8897.35 10125.9 10988.6 13250.8 15328.6 13663.8
classe 5    8677.3 9294.36 10677.6 11816 14549.2 17128.8 15144
classe 6    9037.58 9691.38 11229.3 12643.5 15847.6 18928.9 16624.2
classe 7    9397.86 10088.4 11781 13470.9 17145.9 20729.1 18104.4
classe 8    9758.14 10485.4 12332.6 14298.4 18444.3 22529.2 19584.6
classe 9    10118.4 10882.4 12884.3 15125.8 19742.7 24329.3 21064.8
classe 10   10478.7 11279.4 13436 15953.3 21041 26129.5 22545

class means/stddev for each band

class 1 (2403)
moyennes 7025.72 7388.7 7878.26 7537.53 7520.7 7696.79 7654.33
écart-type 876.124 788.054 722.17 679.73 615.7 351.733 278.397

class 2 (172)
moyennes 8244.99 8643.94 9646.46 9683.51 13048 10536.1 9337.4
écart-type 607.341 538.888 574.945 658.593 1473.34 507.789 685.588

class 3 (54)
moyennes 8434.26 9040.37 10488.3 10949.8 13355.8 12442.6 10824.8
écart-type 1110.78 998.131 932.028 1023.89 1418.08 801.709 1082.7

class 4 (54)
moyennes 8482.3 9044.26 10774 11464.2 14641.1 14702 12465.4
écart-type 907.771 1145.32 855.87 991.749 1398.46 860.045 1151.78

class 5 (108)
```

```
moyennes 8777.68 9379.79 10667.9 11668.6 15965.4 17160.8 14226.1
écart-type 853.549 797.446 671.475 816.731 1669.22 1007.64 1139.25

class 6 (206)
moyennes 8961.07 9666.94 11222.5 12566.3 16796.6 19213.9 15756.8
écart-type 753.46 661.341 727.188 777.205 1234.98 854.702 874.231

class 7 (398)
moyennes 9340.86 10100.9 11741.2 13426.2 17780.8 21026.7 17500.4
écart-type 831.339 799.109 701.629 684.796 833.681 933.273 783.303

class 8 (836)
moyennes 9615.52 10387.7 12217.9 14224.5 18744.5 22966.9 19275.4
écart-type 484.651 457.958 538.072 601.26 827.493 771.913 901.151

class 9 (1315)
moyennes 9896.03 10698.6 12709.9 15019.5 19718.5 24587.7 21016.1
écart-type 457.581 436.544 473.69 548.46 717.103 666.677 920.163

class 10 (1463)
moyennes 10460.6 11305.4 13649.4 16332.8 21077.1 26573.8 23634.1
écart-type 1034.73 1026.42 1039.6 1120.3 1101.26 1037.7 1333.34

Distribution des classes
       2403        172         54         54        108
        206        398        836       1315       1463

######## iteration 1 ############
10 classes, 93.94% points stable
Distribution des classes
       2346        222         61         56        112
        216        412        858       1464       1262

######## iteration 2 ############
10 classes, 95.86% points stable
Distribution des classes
       2327        236         65         58        117
        220        429        909       1527       1121

######## iteration 3 ############
10 classes, 96.66% points stable
Distribution des classes
       2320        242         66         58        118
        233        433        985       1528       1026

######## iteration 4 ############
10 classes, 97.05% points stable
Distribution des classes
       2317        244         67         58        120
        245        450       1035       1522        951

######## iteration 5 ############
10 classes, 97.65% points stable
Distribution des classes
       2315        246         67         58        124
        254        468       1066       1513        898

######## iteration 6 ############
10 classes, 97.87% points stable
Distribution des classes
       2314        246         68         59        126
        262        492       1091       1490        861

######## iteration 7 ############
10 classes, 97.72% points stable
Distribution des classes
       2314        247         67         59        132
        265        527       1108       1468        822

######## iteration 8 ############
10 classes, 97.73% points stable
Distribution des classes
       2314        247         67         60        139
        272        550       1137       1431        792

######## iteration 9 ############
10 classes, 97.82% points stable
Distribution des classes
       2314        247         67         61        148
        283        565       1155       1408        761
```

```
######## iteration 10 ###########
10 classes, 97.87% points stable
Distribution des classes
       2314        247         67         63        159
        288        587       1166       1382        736

######## iteration 11 ###########
10 classes, 97.97% points stable
Distribution des classes
       2314        247         67         65        166
        300        600       1180       1362        708

######## iteration 12 ###########
10 classes, 97.97% points stable
Distribution des classes
       2314        247         67         67        174
        306        618       1199       1336        681

######## iteration 13 ###########
10 classes, 97.82% points stable
Distribution des classes
       2314        247         67         68        183
        320        631       1215       1311        653

######## iteration 14 ###########
10 classes, 97.67% points stable
Distribution des classes
       2314        247         67         71        189
        339        649       1216       1294        623

######## iteration 15 ###########
10 classes, 97.75% points stable
Distribution des classes
       2314        247         67         78        187
        366        664       1214       1271        601

######## iteration 16 ###########
10 classes, 97.86% points stable
Distribution des classes
       2314        247         67         83        191
        375        698       1210       1241        583

######## iteration 17 ###########
10 classes, 97.67% points stable
Distribution des classes
       2314        247         68         84        198
        392        724       1208       1214        560

######## iteration 18 ###########
10 classes, 97.77% points stable
Distribution des classes
       2314        247         69         85        203
        409        744       1220       1180        538

######## iteration 19 ###########
10 classes, 98.13% points stable
Distribution des classes
       2314        246         70         87        207
        420        771       1218       1157        519

########## final results ##############
10 classes (convergence=98.1%)

class separability matrix

        1     2     3     4     5     6     7     8     9    10

  1     0
  2   2.1     0
  3   2.8   0.9     0
  4   3.8   1.6   0.9     0
  5   5.5   2.7   1.8   0.8     0
  6   7.3   3.7   2.6   1.6   0.8     0
  7   9.7   4.9   3.6   2.4   1.7   0.8     0
  8  11.2   5.8   4.3   3.1   2.4   1.5   0.8     0
  9  13.6   6.9   5.2   3.9   3.2   2.4   1.6   0.9     0
 10   9.3   5.9   4.6   3.6   3.1   2.5   2.0   1.4   0.9     0

class means/stddev for each band

class 1 (2314)
```

```
moyennes 6973.65 7333.17 7802.18 7449.64 7428.58 7651.15 7624.97
écart-type 843.931 743.306 609.592 501.577 345.569 249.854 217.016

class 2 (246)
moyennes 8252.11 8657.06 9652.88 9648.4 12056.2 9895.76 8929.32
écart-type 557.912 494.393 540.394 611.288 2106.96 900.212 650.071

class 3 (70)
moyennes 8590.16 9205.93 10637.7 11065.5 12784.4 12166.4 10782.5
écart-type 1067.97 929.601 879.515 980.828 1360.11 857.334 1097.74

class 4 (87)
moyennes 8600 9184.85 10676.8 11445.1 15283.8 15305.9 12848.6
écart-type 912.171 1068.36 783.743 980.84 1744.45 1027.32 1099.21

class 5 (207)
moyennes 8858.84 9488.23 10930.6 12115.5 16366.1 18473.8 15114.5
écart-type 676.137 631.376 684.995 773.703 1487.35 981.082 958.443

class 6 (420)
moyennes 9293.96 10069.1 11712.3 13349.1 17673.2 20665.3 17190.3
écart-type 922.304 860.24 762.823 749.532 931.792 978.143 799.221

class 7 (771)
moyennes 9572.57 10340.5 12145.3 14124.8 18643 22810.7 19095.9
écart-type 469.21 442.231 519.984 585.987 852.925 740.509 837.032

class 8 (1218)
moyennes 9858.67 10659.5 12653.4 14932 19617.3 24380.3 20745.2
écart-type 484.521 463.705 507.611 581.417 763.351 679.252 844.481

class 9 (1157)
moyennes 10151.4 10976 13175.7 15709.2 20443.3 25921.2 22794.1
écart-type 308.902 292.289 375.14 497.641 661.54 633.314 862.877

class 10 (519)
moyennes 10972.1 11840.8 14389.4 17280.3 21993 27486 24867.4
écart-type 1562.41 1542.91 1405.19 1333.89 1222.02 1065.41 1187.97

#################### CLASSES ####################

10 classes, 98.13% points stable

######## CLUSTER END (Fri Jul 28 19:59:34 2023) ########
```

Appendix C.3. Results of the processing of the Landsat 8 OLI/TIRS Image on February 2020

```
Location: Senegal
Mapset:   PERMANENT
Group:    L8_2020f
Subgroup: res_30m
 L8_2020f_01@PERMANENT
 L8_2020f_02@PERMANENT
 L8_2020f_03@PERMANENT
 L8_2020f_04@PERMANENT
 L8_2020f_05@PERMANENT
 L8_2020f_06@PERMANENT
 L8_2020f_07@PERMANENT
Result signature file: cluster_L8_2020f

Region
  North:   1715415.00  East:    435015.00
  South:   1481685.00  West:    209355.00
  Res:          30.00  Res:         30.00
  Rows:          7791  Cols:         7522  Cells: 58603902
Mask: no

Cluster parameters
  Nombre de classes initiales:  10
 Minimum class size:           17
 Minimum class separation:     0.000000
 Percent convergence:          98.000000
 Maximum number of iterations: 30

 Row sampling interval:        77
 Col sampling interval:        75

Sample size: 7019 points

means and standard deviations for 7 bands
```

```
moyennes 9083.83 9752.19 11309.8 12660.8 15669.2 18426 16517.6
écart-type 1543.97 1736.65 2521.06 3917.12 6100.01 8265.57 7020.52

initial means for each band

classe 1    7539.85 8015.54 8788.73 8743.63 9569.16 10160.4 9497.05
classe 2    7882.96 8401.46 9348.96 9614.1 10924.7 11997.2 11057.2
classe 3    8226.06 8787.39 9909.19 10484.6 12280.3 13834 12617.3
classe 4    8569.17 9173.31 10469.4 11355 13635.8 15670.8 14177.4
classe 5    8912.27 9559.23 11029.7 12225.5 14991.4 17507.6 15737.5
classe 6    9255.38 9945.15 11589.9 13096 16347 19344.4 17297.6
classe 7    9598.49 10331.1 12150.1 13966.5 17702.5 21181.1 18857.7
classe 8    9941.59 10717 12710.4 14836.9 19058.1 23017.9 20417.9
classe 9    10284.7 11102.9 13270.6 15707.4 20413.6 24854.7 21978
classe 10   10627.8 11488.8 13830.8 16577.9 21769.2 26691.5 23538.1

class means/stddev for each band

class 1 (2462)
moyennes 7211.87 7635.75 8230.97 7806.78 7768.17 7995.81 7969.81
écart-type 526.693 555.399 717.049 625.503 683.423 368.145 296.641

class 2 (151)
moyennes 8230.97 8631.27 9677.65 9672.28 13741.1 10679 9296.59
écart-type 527.748 570.343 706.969 853.031 1124.61 528.113 423.434

class 3 (37)
moyennes 8907.43 9529.78 11033 11653.5 13593.8 13001.9 11181
écart-type 702.35 683.603 1186.27 1550.73 971.094 1016.7 872.869

class 4 (52)
moyennes 8996.48 9559.69 10903.2 11524.1 15370.3 15205.8 12684.4
écart-type 798.4 847.117 1087.63 1263.82 1549.33 897.804 926.343

class 5 (118)
moyennes 8988.28 9631.89 11060.3 12112.4 16470.8 17744.5 14596.6
écart-type 724.575 766.586 903.884 1007.71 1483.12 1171.72 919.712

class 6 (212)
moyennes 9239.58 9942.75 11523.7 12951.1 17223.6 19755.3 16495.6
écart-type 641.91 639.603 760.009 816.876 1108.93 971.252 835.724

class 7 (427)
moyennes 9520.33 10286 12035.1 13822.2 18250.7 21545.8 18263.6
écart-type 530.374 535.672 683.599 748.033 995.498 910.479 1078.38

class 8 (790)
moyennes 9846.31 10634 12513 14635.6 19310.4 23432.2 20130.1
écart-type 393.007 413.585 577.216 679.58 1011.3 729.564 1139.33

class 9 (1126)
moyennes 10185.5 11022 13135.2 15626.8 20457.7 25120.9 21898.5
écart-type 319.918 338.3 471.731 586.261 961.045 652.206 1145.82

class 10 (1644)
moyennes 10724.7 11587.7 14063 16982.8 21776.8 27057.3 24488.8
écart-type 475.297 518.812 729.047 925.558 919.804 968.935 1491.99

Distribution des classes
       2462        151         37         52        118
        212        427        790       1126       1644

######## iteration 1 ############
10 classes, 93.96% points stable
Distribution des classes
       2417        190         46         58        118
        224        414        803       1347       1402

######## iteration 2 ############
10 classes, 95.81% points stable
Distribution des classes
       2404        203         44         64        127
        228        417        854       1426       1252

######## iteration 3 ############
10 classes, 96.68% points stable
Distribution des classes
       2400        206         45         66        135
        230        439        897       1440       1161
```

```
######## iteration 4 ###########
10 classes, 97.01% points stable
Distribution des classes
       2396        210         46         71        135
        237        472        911       1454       1087

######## iteration 5 ###########
10 classes, 97.22% points stable
Distribution des classes
       2394        212         46         75        140
        248        491        931       1453       1029

######## iteration 6 ###########
10 classes, 97.51% points stable
Distribution des classes
       2394        212         48         74        145
        270        506        940       1442        988

######## iteration 7 ###########
10 classes, 97.45% points stable
Distribution des classes
       2394        211         51         73        150
        290        535        927       1447        941

######## iteration 8 ###########
10 classes, 97.54% points stable
Distribution des classes
       2393        210         54         75        154
        312        551        939       1419        912

######## iteration 9 ###########
10 classes, 97.63% points stable
Distribution des classes
       2392        210         55         78        157
        337        562        951       1394        883

######## iteration 10 ###########
10 classes, 97.99% points stable
Distribution des classes
       2391        211         56         80        159
        353        576        965       1371        857

######## iteration 11 ###########
10 classes, 98.15% points stable
Distribution des classes
       2391        211         56         83        159
        367        598        972       1348        834

########## final results #############
10 classes (convergence=98.1%)

class separability matrix

        1     2     3     4     5     6     7     8     9    10

  1     0
  2   1.9     0
  3   2.7   1.0     0
  4   3.9   2.1   0.9     0
  5   6.1   3.1   1.6   0.9     0
  6   6.6   3.9   2.2   1.4   1.0     0
  7   8.5   5.1   2.9   2.2   1.8   0.7     0
  8   9.7   5.9   3.5   2.8   2.6   1.4   0.8     0
  9  11.5   7.2   4.3   3.6   3.6   2.2   1.6   0.8     0
 10  11.0   7.3   4.7   4.0   4.1   2.8   2.3   1.6   0.9     0

class means/stddev for each band

class 1 (2391)
moyennes 7174.13 7597.81 8180.06 7743.75 7681.17 7961.31 7950.84
écart-type 474.355 506.243 651.214 496.461 399.352 301.276 273.692

class 2 (211)
moyennes 8265.83 8662.6 9678.62 9648.93 12791.6 10147.2 9043.17
écart-type 474.465 474.914 566.938 690.234 1903.84 857.025 485.482

class 3 (56)
moyennes 9047.8 9694.07 11237.7 11844.9 13414.8 12763.5 10983.3
écart-type 842.033 869.921 1189.56 1403.88 1106.82 1314.85 1024.01

class 4 (83)
```

```
moyennes 9380.73 10028 11507.2 12260.1 16175.5 15868 13405.5
écart-type 1038.06 1114.75 1325.39 1632.15 1924.21 859.971 1121.43

class 5 (159)
moyennes 8836.65 9450.75 10813.8 11997.1 16565.9 18847.2 15422.1
écart-type 403.779 359.336 415.253 545.655 1077.34 877.599 906.505

class 6 (367)
moyennes 9423.02 10182.4 11899.3 13572.1 17943 20712.5 17364.6
écart-type 612.1 615.543 754.174 823.19 1058.68 992.025 889.261

class 7 (598)
moyennes 9674.92 10440.4 12239.9 14200.3 18780.9 22750.7 19495.3
écart-type 384.698 387.804 541.838 641.686 1023.19 770.277 1025.82

class 8 (972)
moyennes 10047.9 10871.7 12888.1 15256.2 20058.7 24396.6 21007.5
écart-type 343.349 369.808 518.198 630.15 1057.62 740.142 1126.64

class 9 (1348)
moyennes 10407.7 11254.2 13522.1 16201.9 21042 26036.4 23049.6
écart-type 336.99 361.142 501.239 651.252 880.583 671.315 987.174

class 10 (834)
moyennes 10949.2 11823 14433.3 17487.2 22196.4 27709.5 25560.3
écart-type 491.77 547.304 748.697 934.506 897.309 844.818 1136.09

#################### CLASSES ####################

10 classes, 98.15% points stable

######## CLUSTER END (Fri Jul 28 18:25:15 2023) ########
```

Appendix C.4. Results of the processing of the Landsat 8 OLI/TIRS Image on February 2021

```
Location: Senegal
Mapset:   PERMANENT
Group:    L8_2021f
Subgroup: res_30m
 L8_2021f_01@PERMANENT
 L8_2021f_02@PERMANENT
 L8_2021f_03@PERMANENT
 L8_2021f_04@PERMANENT
 L8_2021f_05@PERMANENT
 L8_2021f_06@PERMANENT
 L8_2021f_07@PERMANENT
Result signature file: cluster_L8_2021f

Region
  North:   1715415.00  East:    435015.00
  South:   1481685.00  West:    209355.00
  Res:          30.00  Res:         30.00
  Rows:          7791  Cols:         7522  Cells: 58603902
Mask: no

Cluster parameters
  Nombre de classes initiales:  10
 Minimum class size:           17
 Minimum class separation:     0.000000
 Percent convergence:          98.000000
 Maximum number of iterations: 30

 Row sampling interval:        77
 Col sampling interval:        75

Sample size: 7018 points

means and standard deviations for 7 bands

moyennes 9103.03 9794.56 11362.2 12712.1 15680.1 18312.7 16272.1
écart-type 1494.79 1731.05 2554.95 3927.55 6122.9 8260.3 6924.15

initial means for each band

classe 1    7608.24 8063.5 8807.27 8784.6 9557.25 10052.4 9347.93
classe 2    7940.42 8448.18 9375.03 9657.39 10917.9 11888 10886.6
classe 3    8272.59 8832.86 9942.8 10530.2 12278.5 13723.6 12425.3
classe 4    8604.77 9217.54 10510.6 11403 13639.2 15559.3 13964
classe 5    8936.94 9602.22 11078.3 12275.8 14999.8 17394.9 15502.7
classe 6    9269.12 9986.9 11646.1 13148.5 16360.5 19230.5 17041.4
```

```
classe 7    9601.29 10371.6 12213.9 14021.3 17721.1 21066.1 18580.1
classe 8    9933.47 10756.3 12781.6 14894.1 19081.8 22901.8 20118.8
classe 9    10265.6 11140.9 13349.4 15766.9 20442.4 24737.4 21657.5
classe 10   10597.8 11525.6 13917.2 16639.7 21803 26573 23196.2

class means/stddev for each band

class 1 (2472)
moyennes 7313.61 7696.41 8232.04 7837.92 7742.14 7931.25 7880.26
écart-type 523.008 574.873 740.83 667.615 597.157 326.44 221.817

class 2 (162)
moyennes 8367.74 8788.43 9871.6 9907.87 13579.2 10720.3 9384.91
écart-type 551.281 578.474 738.688 868.216 1280.37 510.118 395.672

class 3 (39)
moyennes 8860.13 9479.1 10889.1 11353.3 14026.3 12695 11036.6
écart-type 995.855 1068.1 1280.86 1258.34 1432.8 987.66 940.02

class 4 (52)
moyennes 8990.67 9572.25 10911.4 11588.4 15314.2 15146.8 12747.7
écart-type 1053.52 1085.71 1273.12 1320.13 1385.28 1102.05 995.233

class 5 (111)
moyennes 8919.6 9586.4 11049.8 12041.2 16704.5 17443.7 14294.6
écart-type 772.356 773.025 855.924 967.103 1465.14 1107.34 861.372

class 6 (191)
moyennes 9221.2 9972.19 11635.4 13050.4 17569.3 19529.4 16048.3
écart-type 760.844 777.297 906.372 985.172 1371.94 1015.06 961.004

class 7 (375)
moyennes 9554.95 10380.6 12217.9 13998.3 18422.8 21362.9 17907.5
écart-type 676.841 675.041 824.381 903.755 1005.47 983.878 1008.25

class 8 (768)
moyennes 9829.27 10696.1 12661.2 14797.4 19473.4 23316.6 19666.1
écart-type 428.049 420.829 530.225 620.714 878.759 770.735 1045.84

class 9 (1262)
moyennes 10151.2 11058.1 13225.5 15720.3 20503.2 25045.5 21495.6
écart-type 369.177 375.082 483.879 587.818 844.55 650.355 1165.65

class 10 (1586)
moyennes 10682.9 11595.3 14094.6 16964.8 21697.6 26923.8 24278.5
écart-type 477.378 511.286 708.716 895.261 882.054 904.887 1404.13

Distribution des classes
       2472        162         39         52        111
        191        375        768       1262       1586

######## iteration 1 ############
10 classes, 93.84% points stable
Distribution des classes
       2412        222         40         50        122
        190        391        798       1414       1379

######## iteration 2 ############
10 classes, 95.97% points stable
Distribution des classes
       2385        252         33         59        118
        203        399        859       1451       1259

######## iteration 3 ############
10 classes, 97.16% points stable
Distribution des classes
       2375        263         30         64        117
        213        419        892       1454       1191

######## iteration 4 ############
10 classes, 97.52% points stable
Distribution des classes
       2368        270         29         72        110
        222        439        921       1457       1130

######## iteration 5 ############
10 classes, 97.38% points stable
Distribution des classes
       2366        272         28         77        109
        232        474        930       1452       1078
```

```
######## iteration 6 ###########
10 classes, 97.65% points stable
Distribution des classes
       2364        274         28         78        111
        242        500        954       1433       1034

######## iteration 7 ###########
10 classes, 97.82% points stable
Distribution des classes
       2363        275         28         79        114
        256        527        959       1417       1000

######## iteration 8 ###########
10 classes, 97.86% points stable
Distribution des classes
       2363        275         28         80        120
        266        554        967       1394        971

######## iteration 9 ###########
10 classes, 97.99% points stable
Distribution des classes
       2363        275         28         83        128
        277        568        979       1367        950

######## iteration 10 ###########
10 classes, 98.03% points stable
Distribution des classes
       2363        275         29         84        136
        285        586        986       1352        922

########## final results ##############
10 classes (convergence=98.0%)

class separability matrix

        1     2     3     4     5     6     7     8     9    10

  1     0
  2   2.0     0
  3   2.8   1.0     0
  4   4.0   1.7   0.9     0
  5   5.8   2.4   1.6   0.7     0
  6   6.2   3.1   2.0   1.3   0.9     0
  7   9.2   4.4   2.9   2.1   1.8   0.7     0
  8  10.9   5.4   3.6   2.8   2.6   1.4   0.8     0
  9  13.4   6.5   4.4   3.6   3.6   2.1   1.6   0.8     0
 10  12.6   6.8   4.8   4.0   4.0   2.7   2.3   1.6   1.0     0

class means/stddev for each band

class 1 (2363)
moyennes 7248.41 7625.27 8135.66 7730.27 7642.36 7879.37 7847.06
écart-type 416.1 461.809 582.787 424.33 314.927 198.22 146.336

class 2 (275)
moyennes 8476.43 8932.59 10007 9975.02 12183.4 10106.5 9101
écart-type 538.712 566.342 673.216 745.985 2196.19 1014.59 587.313

class 3 (29)
moyennes 9693.86 10405.4 12096.4 12615.7 13407.4 12209.3 10704
écart-type 1489.42 1526.72 1577.5 1226.12 1259.09 1301.44 920.006

class 4 (84)
moyennes 9118.45 9712.07 11054 11807.6 15279.8 15479 13169.4
écart-type 847.439 899.74 1128.4 1347.33 1213.07 1068.09 1063.26

class 5 (136)
moyennes 8654.04 9337.13 10847.5 11891.2 17562.1 18244.7 14672.5
écart-type 419.602 378.092 402.881 617.514 1690.72 1120.92 910.851

class 6 (285)
moyennes 9482.41 10268.2 12016.5 13608.5 17771.1 20200.2 16810.6
écart-type 823.372 837.363 1022.37 1097.31 1217.51 1136.29 1023.16

class 7 (586)
moyennes 9664.83 10504.9 12390.8 14355.7 18922 22427.3 18858.6
écart-type 494.386 484.571 577.002 639.285 909.522 843.101 1002.59

class 8 (986)
moyennes 10011.5 10920.3 13011.5 15386.7 20210.8 24268.9 20383.3
écart-type 432.35 438.117 562.814 669.664 896.054 758.305 925.124
```

```
class 9 (1352)
moyennes 10313.4 11212.2 13478.1 16085.4 20837.1 25786.6 22669.8
écart-type 307.442 315.031 441.953 601.243 875.44 643.19 969.061

class 10 (922)
moyennes 10868.6 11786.6 14394.2 17374.8 22039.6 27432.4 25108.8
écart-type 499.141 546.18 733.711 900.124 851.524 791.249 1102.95

#################### CLASSES ####################

10 classes, 98.03% points stable

######## CLUSTER END (Fri Jul 28 19:30:36 2023) ########
```

Appendix C.5. Results of the processing of the Landsat 9 OLI/TIRS Image on February 2022

```
Location: Senegal
Mapset:   PERMANENT
Group:    L8_2022f
Subgroup: res_30m
 L8_2022f_01@PERMANENT
 L8_2022f_02@PERMANENT
 L8_2022f_03@PERMANENT
 L8_2022f_04@PERMANENT
 L8_2022f_05@PERMANENT
 L8_2022f_06@PERMANENT
 L8_2022f_07@PERMANENT
Result signature file: cluster_L8_2022f

Region
  North:   1715145.00  East:    435015.00
  South:   1481685.00  West:    209355.00
  Res:          30.00  Res:         30.00
  Rows:          7782  Cols:         7522  Cells: 58536204
Mask: no

Cluster parameters
  Nombre de classes initiales:  10
 Minimum class size:           17
 Minimum class separation:     0.000000
 Percent convergence:          98.000000
 Maximum number of iterations: 30

 Row sampling interval:        77
 Col sampling interval:        75

Sample size: 7041 points

means and standard deviations for 7 bands

moyennes 8956.71 9688.81 11275.1 12528.6 15363.6 18204.7 16340.9
écart-type 1511.52 1718.3 2416.99 3735.33 5813.88 8173 7014.93

initial means for each band

classe 1    7445.19 7970.5 8858.07 8793.25 9549.73 10031.7 9325.94
classe 2    7781.08 8352.35 9395.18 9623.32 10841.7 11848 10884.8
classe 3    8116.98 8734.19 9932.29 10453.4 12133.7 13664.2 12443.7
classe 4    8452.87 9116.04 10469.4 11283.5 13425.7 15480.4 14002.6
classe 5    8788.76 9497.88 11006.5 12113.5 14717.6 17296.6 15561.4
classe 6    9124.66 9879.73 11543.6 12943.6 16009.6 19112.9 17120.3
classe 7    9460.55 10261.6 12080.7 13773.7 17301.6 20929.1 18679.2
classe 8    9796.45 10643.4 12617.8 14603.8 18593.6 22745.3 20238.1
classe 9    10132.3 11025.3 13154.9 15433.8 19885.5 24561.5 21796.9
classe 10   10468.2 11407.1 13692 16263.9 21177.5 26377.7 23355.8

class means/stddev for each band

class 1 (2499)
moyennes 7149.81 7606.11 8327.64 7934.83 7897.52 8088.78 7974.9
écart-type 476.729 530.897 654.697 572.875 544.465 242.083 133.289

class 2 (177)
moyennes 8366.47 8874.42 9974.55 10024.6 13424.4 10727.8 9321.19
écart-type 480.74 474.197 597.638 749.492 998.659 442.422 297.4

class 3 (44)
moyennes 8977.66 9664.75 11152.6 11719.6 14047.7 12299.9 10322
écart-type 929.913 925.424 974.416 1071.45 935.147 695.042 524.734
```

```
class 4 (57)
moyennes 8973.72 9634.61 11008.9 11676 15389 15103.2 12441.3
écart-type 1178.34 1172.76 1286.07 1292.94 1304.08 1079.66 1085.64

class 5 (118)
moyennes 8716.79 9452.54 10918.9 11928 16323.4 17608.6 14432.4
écart-type 590.858 512.119 543.432 701.413 1159.46 820.033 896.658

class 6 (236)
moyennes 9167.5 9967.39 11607.4 12914.8 17126.9 19303 16103.9
écart-type 697.739 661.239 686.203 750.139 1032.78 965.321 803.594

class 7 (420)
moyennes 9447.76 10301.8 12089.2 13762.9 18023.4 21262.5 17926.6
écart-type 558.716 522.992 595.324 651.946 809.997 868.978 912.509

class 8 (691)
moyennes 9809.44 10698.2 12615.3 14572.7 18869.4 23083.1 19899
écart-type 555.148 530.208 604.799 692.872 786.72 826.893 954.473

class 9 (1048)
moyennes 10013.8 10930.4 13014.9 15326.5 19885 24925.2 21760.2
écart-type 449.179 412.151 437.629 544.111 717.896 650.93 926.959

class 10 (1751)
moyennes 10494.8 11435.8 13838.4 16597 21217.4 26858.5 24400.9
écart-type 532.17 537.28 701.184 909.995 921.828 954.891 1374.72

Distribution des classes
       2499        177         44         57        118
        236        420        691       1048       1751

######## iteration 1 ############
10 classes, 93.75% points stable
Distribution des classes
       2446        219         59         57        130
        231        429        698       1271       1501

######## iteration 2 ############
10 classes, 95.48% points stable
Distribution des classes
       2418        246         62         61        135
        238        430        752       1358       1341

######## iteration 3 ############
10 classes, 96.07% points stable
Distribution des classes
       2398        265         64         65        133
        255        436        794       1423       1208

######## iteration 4 ############
10 classes, 96.49% points stable
Distribution des classes
       2388        271         69         66        140
        262        454        819       1476       1096

######## iteration 5 ############
10 classes, 96.69% points stable
Distribution des classes
       2384        269         75         68        148
        271        471        855       1488       1012

######## iteration 6 ############
10 classes, 97.06% points stable
Distribution des classes
       2373        275         80         68        158
        284        488        871       1492        952

######## iteration 7 ############
10 classes, 97.12% points stable
Distribution des classes
       2361        274         92         71        164
        292        523        873       1486        905

######## iteration 8 ############
10 classes, 96.79% points stable
Distribution des classes
       2355        258        113         74        178
        292        561        888       1457        865

######## iteration 9 ############
```

```
10 classes, 96.45% points stable
Distribution des classes
       2343        211        169         79        186
        308        572        908       1444        821

######## iteration 10 ###########
10 classes, 96.65% points stable
Distribution des classes
       2318        193        210         82        192
        324        583        934       1423        782

######## iteration 11 ###########
10 classes, 97.40% points stable
Distribution des classes
       2292        211        215         85        197
        343        586        960       1407        745

######## iteration 12 ###########
10 classes, 97.80% points stable
Distribution des classes
       2284        215        215         87        205
        356        589        995       1383        712

######## iteration 13 ###########
10 classes, 98.30% points stable
Distribution des classes
       2280        217        215         85        215
        366        599       1005       1371        688

########## final results ##############
10 classes (convergence=98.3%)

class separability matrix

        1     2     3     4     5     6     7     8     9    10

  1     0
  2   1.9     0
  3   3.4   1.4     0
  4   3.9   2.4   1.3     0
  5   6.8   4.2   2.7   0.8     0
  6   9.0   5.6   3.8   1.5   0.9     0
  7  10.8   6.8   4.7   2.2   1.6   0.8     0
  8  13.0   8.2   5.8   2.9   2.5   1.6   0.8     0
  9  17.2  10.3   7.3   3.7   3.5   2.6   1.8   0.9     0
 10  14.2   9.7   7.2   4.0   3.9   3.2   2.4   1.7   1.0     0

class means/stddev for each band

class 1 (2280)
moyennes 7025.48 7464.39 8158.28 7778.01 7761.86 8031.61 7946.13
écart-type 178.779 226.943 324.92 184.599 131.481 79.2823 57.5162

class 2 (217)
moyennes 8478.77 9119.74 10140.9 9614.1 9235.62 8685.39 8285.76
écart-type 679.055 564.86 649.425 743.536 854.907 480.424 295.583

class 3 (215)
moyennes 8427.28 8962.44 10114.7 10244.3 13546.1 10937.7 9454.59
écart-type 589.808 616.69 783.836 1006.66 898.821 722.578 510.69

class 4 (85)
moyennes 8974.04 9646.82 11063 11772.7 15562.5 15252 12472.7
écart-type 1091.02 1070.91 1170.3 1258.08 1317.05 1278.05 1152.57

class 5 (215)
moyennes 8894.27 9662.64 11198.8 12319.1 16667.8 18360.8 15174.8
écart-type 650.006 601.662 640.83 740.228 1243.47 914.766 855.948

class 6 (366)
moyennes 9363.72 10204.3 11954.8 13520 17753.4 20518.5 17151.1
écart-type 642.708 608.057 663.767 714.718 885.718 931.806 745.633

class 7 (599)
moyennes 9692.46 10568.2 12430.5 14297.5 18566.7 22456.7 19229.1
écart-type 512.937 502.549 626.257 724.265 846.028 818.41 826.925

class 8 (1005)
moyennes 9949.63 10862.3 12901.4 15109.7 19602.2 24435.6 21202.7
écart-type 527.455 484.451 494.992 618.607 810.149 750.457 868.985
```

```
class 9 (1371)
moyennes 10245.7 11177.4 13428.2 15984.8 20603.3 26095.9 23331.5
écart-type 331.531 317.553 397.462 511.39 639.139 608.235 870.287

class 10 (688)
moyennes 10814.1 11759.8 14340.3 17338.4 21931.3 27748 25717.5
écart-type 623.912 645.156 793.88 948.838 928.213 772.474 992.741

#################### CLASSES ####################

10 classes, 98.30% points stable

######## CLUSTER END (Fri Jul 28 19:40:07 2023) ########
```

Appendix C.6. Results of the processing of the Landsat 9 OLI/TIRS Image on February 2023

```
Location: Senegal
Mapset:   PERMANENT
Group:    L8_2023f
Subgroup: res_30m
 L8_2023f_01@PERMANENT
 L8_2023f_02@PERMANENT
 L8_2023f_03@PERMANENT
 L8_2023f_04@PERMANENT
 L8_2023f_05@PERMANENT
 L8_2023f_06@PERMANENT
 L8_2023f_07@PERMANENT
Result signature file: cluster_L8_2023f

Region
  North:   1715145.00  East:    435015.00
  South:   1481685.00  West:    209355.00
  Res:          30.00  Res:         30.00
  Rows:          7782  Cols:         7522  Cells: 58536204
Mask: no

Cluster parameters
  Nombre de classes initiales:  10
 Minimum class size:           17
 Minimum class separation:     0.000000
 Percent convergence:          98.000000
 Maximum number of iterations: 30

 Row sampling interval:        77
 Col sampling interval:        75

Sample size: 7040 points

means and standard deviations for 7 bands

moyennes 8748.83 9249.98 10407.4 11511.3 14630.9 16933.1 14828.1
écart-type 1191.3 1448.72 2255.67 3457.16 5679.26 7632.14 6217.75

initial means for each band

classe 1    7557.53 7801.27 8151.69 8054.12 8951.65 9300.92 8610.34
classe 2    7822.27 8123.2 8652.95 8822.38 10213.7 10997 9992.06
classe 3    8087 8445.14 9154.21 9590.64 11475.8 12693 11373.8
classe 4    8351.73 8767.08 9655.47 10358.9 12737.8 14389 12755.5
classe 5    8616.47 9089.02 10156.7 11127.2 13999.9 16085 14137.2
classe 6    8881.2 9410.95 10658 11895.4 15261.9 17781.1 15518.9
classe 7    9145.93 9732.89 11159.3 12663.7 16524 19477.1 16900.7
classe 8    9410.67 10054.8 11660.5 13431.9 17786.1 21173.1 18282.4
classe 9    9675.4 10376.8 12161.8 14200.2 19048.1 22869.2 19664.1
classe 10   9940.13 10698.7 12663 14968.4 20310.2 24565.2 21045.8

class means/stddev for each band

class 1 (2496)
moyennes 7397.33 7594.23 7783.32 7379.16 7315.58 7469.63 7457.21
écart-type 257.134 379.462 656.612 476.84 486.298 184.185 103.77

class 2 (158)
moyennes 7876.46 8178.05 9049.89 8908.23 12997.6 9679.61 8534.34
écart-type 525.091 609.018 853.878 1046.68 1198.88 489.001 400.555

class 3 (36)
moyennes 8382.67 8870.58 10132.7 10466.1 13936.5 11387.3 9487.14
écart-type 947.565 1065.53 1372.44 1691.4 1632.83 953.406 696.225
```

```
class 4 (57)
moyennes 8251.86 8600.88 9571.46 9959.93 15437 14481.2 11342.6
écart-type 533.787 587.414 837.827 1029.4 1271.36 860 557.976

class 5 (134)
moyennes 8416.31 8815.56 9833.32 10574.2 15771.8 16461.1 13140.7
écart-type 406.687 433.512 557.12 723.845 1367.17 906.857 862.696

class 6 (266)
moyennes 8708.59 9204.28 10390.3 11470 16474.1 18107.3 14574.8
écart-type 475.259 531.153 700.063 818.458 1227.04 969.829 863.811

class 7 (443)
moyennes 9099.78 9692.12 11043.4 12467 17136.3 19840.7 16357.9
écart-type 568.161 626.07 793.584 804.164 936.815 918.436 828.39

class 8 (737)
moyennes 9302.5 9950.57 11478.8 13254.1 18110 21558.5 17941.3
écart-type 374.83 425.163 583.044 633.254 877.581 798.585 957.001

class 9 (1139)
moyennes 9569.47 10281.3 11997.1 14137.3 19165.5 23156.4 19494.1
écart-type 401.813 455.841 596 639.838 825.612 693.586 1018.06

class 10 (1574)
moyennes 10089.2 10861.3 12962 15506.7 20357.8 25237.8 22318.4
écart-type 634.665 725.644 1032.03 1216.96 1066.29 1182.48 1657.15

Distribution des classes
       2496        158         36         57        134
        266        443        737       1139       1574

######## iteration 1 ############
10 classes, 92.90% points stable
Distribution des classes
       2457        189         47         67        139
        262        463        736       1386       1294

######## iteration 2 ############
10 classes, 94.94% points stable
Distribution des classes
       2456        190         46         77        150
        265        461        799       1489       1107

######## iteration 3 ############
10 classes, 95.65% points stable
Distribution des classes
       2456        189         46         81        170
        258        486        853       1514        987

######## iteration 4 ############
10 classes, 96.08% points stable
Distribution des classes
       2457        187         47         85        181
        269        506        908       1495        905

######## iteration 5 ############
10 classes, 96.83% points stable
Distribution des classes
       2457        186         47         91        190
        269        541        948       1455        856

######## iteration 6 ############
10 classes, 97.09% points stable
Distribution des classes
       2457        180         53         91        199
        285        564        970       1432        809

######## iteration 7 ############
10 classes, 97.64% points stable
Distribution des classes
       2456        178         56         91        204
        296        579       1010       1401        769

######## iteration 8 ############
10 classes, 97.64% points stable
Distribution des classes
       2454        174         61         92        207
        305        597       1051       1373        726

######## iteration 9 ############
```

```
10 classes, 97.68% points stable
Distribution des classes
       2454        169         63         96        212
        316        615       1081       1339        695

######## iteration 10 ###########
10 classes, 97.74% points stable
Distribution des classes
       2451        165         70         96        222
        322        633       1110       1303        668

######## iteration 11 ###########
10 classes, 98.07% points stable
Distribution des classes
       2447        164         75         96        228
        337        643       1128       1276        646

########## final results ##############
10 classes (convergence=98.1%)

class separability matrix

        1     2     3     4     5     6     7     8     9    10

  1     0
  2   3.0     0
  3   2.0   1.1     0
  4   4.3   1.9   1.3     0
  5   6.2   3.3   1.9   0.9     0
  6   8.3   4.5   2.5   1.8   0.8     0
  7   8.6   4.9   2.9   2.3   1.4   0.8     0
  8  11.1   6.4   3.7   3.2   2.3   1.6   0.7     0
  9  12.9   7.6   4.3   4.0   3.1   2.5   1.5   0.8     0
 10   9.8   6.6   4.3   4.0   3.3   2.8   2.0   1.5   0.9     0

class means/stddev for each band

class 1 (2447)
moyennes 7384.68 7577.4 7750.19 7338.65 7256.2 7449.93 7447.4
écart-type 233.526 354.406 605.312 359.398 190.13 96.7428 65.728

class 2 (164)
moyennes 7768.28 8005.41 8737.76 8518.4 13138.8 9607.03 8456.8
écart-type 205.996 186.285 242.11 330.13 1262.87 607.591 379.622

class 3 (75)
moyennes 8525.51 9128.15 10591.1 10928.9 11174.8 9722.17 8725.32
écart-type 918.434 942.837 1086.16 1169.19 1692.48 1530.59 939.662

class 4 (96)
moyennes 8163.46 8518.08 9519.66 9865.24 16131.8 14749.6 11550
écart-type 412.115 431.61 583.174 750.222 1677.81 1030.87 735.6

class 5 (228)
moyennes 8568.15 9033.46 10155.7 11075.6 16134 17188.2 13740.3
écart-type 483.059 558.081 776.923 904.11 1382.8 872.156 678.826

class 6 (337)
moyennes 8871.33 9394.43 10612 11902 16595.4 19221.5 15596.3
écart-type 402.996 432.52 557.997 635.147 984.32 833.374 715.065

class 7 (643)
moyennes 9260.18 9891.57 11366 12992.1 17749 20723.4 17203.5
écart-type 521.521 573.699 738.973 756.273 952.239 979.531 836.2

class 8 (1128)
moyennes 9463.09 10163.8 11815.7 13862 18902.5 22691.9 18913.4
écart-type 380.886 443.357 597.014 679.936 942.091 744.636 887.704

class 9 (1276)
moyennes 9787.57 10519.4 12406.4 14745.2 19700.1 24299.8 21058.5
écart-type 334.318 380.658 525.448 612.7 810.222 749.323 968.629

class 10 (646)
moyennes 10470 11283.8 13627.1 16372.5 20992.3 26212.4 23777.5
écart-type 775.83 898.648 1231.43 1389.82 1174.18 1099.88 1360.82

##################### CLASSES ####################

10 classes, 98.07% points stable
```

```
######## CLUSTER END (Fri Jul 28 19:46:42 2023) ########
```

References

1. Karra, K.; Kontgis, C.; Statman-Weil, Z.; Mazzariello, J.C.; Mathis, M.; Brumby, S.P. Global land use/land cover with Sentinel 2 and deep learning. In Proceedings of the 2021 IEEE International Geoscience and Remote Sensing Symposium IGARSS, Brussels, Belgium, 11–16 July 2021; pp. 4704–4707. https://doi.org/10.1109/IGARSS47720.2021.9553499.
2. Ngom, N.M.; Mbaye, M.; Baratoux, D.; Baratoux, L.; Catry, T.; Dessay, N.; Faye, G.; Sow, E.H.; Delaitre, E. Mapping Artisanal and Small-Scale Gold Mining in Senegal Using Sentinel 2 Data. *GeoHealth* **2020**, *4*, e2020GH000310. https://doi.org/10.1029/2020GH000310.
3. Tong, X.; Brandt, M.; Hiernaux, P.; Herrmann, S.; Rasmussen, L.V.; Rasmussen, K.; Tian, F.; Tagesson, T.; Zhang, W.; Fensholt, R. The forgotten land use class: Mapping of fallow fields across the Sahel using Sentinel-2. *Remote Sens. Environ.* **2020**, *239*, 111598. https://doi.org/10.1016/j.rse.2019.111598.
4. Konarska, K.M.; Sutton, P.C.; Castellon, M. Evaluating scale dependence of ecosystem service valuation: A comparison of NOAA-AVHRR and Landsat TM datasets. *Ecol. Econ.* **2002**, *41*, 491–507. https://doi.org/10.1016/S0921-8009(02)00096-4.
5. Anyamba, A.; Tucker, C. Analysis of Sahelian vegetation dynamics using NOAA-AVHRR NDVI data from 1981–2003. *J. Arid Environ.* **2005**, *63*, 596–614. https://doi.org/10.1016/j.jaridenv.2005.03.007.
6. Frederiksen, P.; Lawesson, J.E. Vegetation types and patterns in Senegal based on multivariate analysis of field and NOAA-AVHRR satellite data. *J. Veg. Sci.* **1992**, *3*, 535–544. https://doi.org/10.2307/3235810.
7. Silva, J.M.; Sá, A.C.; Pereira, J.M. Comparison of burned area estimates derived from SPOT-VEGETATION and Landsat ETM+ data in Africa: Influence of spatial pattern and vegetation type. *Remote Sens. Environ.* **2005**, *96*, 188–201. https://doi.org/10.1016/j.rse.2005.02.004.
8. Martínez, B.; Gilabert, M.; García-Haro, F.; Faye, A.; Meliá, J. Characterizing land condition variability in Ferlo, Senegal (2001–2009) using multi-temporal 1-km Apparent Green Cover (AGC) SPOT Vegetation data. *Glob. Planet. Chang.* **2011**, *76*, 152–165. https://doi.org/10.1016/j.gloplacha.2011.01.001.
9. Pimple, U.; Simonetti, D.; Hinks, I.; Oszwald, J.; Berger, U.; Pungkul, S.; Leadprathom, K.; Pravinvongvuthi, T.; Maprasoap, P.; Gond, V. A history of the rehabilitation of mangroves and an assessment of their diversity and structure using Landsat annual composites (1987–2019) and transect plot inventories. *For. Ecol. Manag.* **2020**, *462*, 118007. https://doi.org/10.1016/j.foreco.2020.118007.
10. Lemenkova, P. Mapping Wetlands of Kenya Using Geographic Resources Analysis Support System (GRASS GIS) with Remote Sensing Data. *Transylv. Rev. Syst. Ecol. Res.* **2023**, *25*, 1–18. https://doi.org/10.2478/trser-2023-0008.
11. Ogilvie, A.; Poussin, J.C.; Bader, J.C.; Bayo, F.; Bodian, A.; Dacosta, H.; Dia, D.; Diop, L.; Martin, D.; Sambou, S. Combining Multi-Sensor Satellite Imagery to Improve Long-Term Monitoring of Temporary Surface Water Bodies in the Senegal River Floodplain. *Remote Sens.* **2020**, *12*, 3157. https://doi.org/10.3390/rs12193157.
12. Mayaux, P.; Bartholomé, E.; Fritz, S.; Belward, A. A new land-cover map of Africa for the year 2000. *J. Biogeogr.* **2004**, *31*, 861–877. https://doi.org/10.1111/j.1365-2699.2004.01073.x.
13. Karra, K.; Kontgis, C.; Statman-Weil, Z.; Mazzariello, J.C.; Mathis, M.; Brumby, S.P. ESRI 10m Annual Land Cover (2017–2023). 2024. Available online: https://gee-community-catalog.org/projects/S2TSLULC/#class-definitions (accessed on 2 July 2024) .
14. Acker, J.; Williams, R.; Chiu, L.; Ardanuy, P.; Miller, S.; Schueler, C.; Vachon, P.; Manore, M. Remote Sensing from Satellites. In *Reference Module in Earth Systems and Environmental Sciences*; Elsevier: Amsterdam, The Netherlands, 2014. https://doi.org/10.1016/B978-0-12-409548-9.09440-9.
15. Hakimdavar, R.; Hubbard, A.; Policelli, F.; Pickens, A.; Hansen, M.; Fatoyinbo, T.; Lagomasino, D.; Pahlevan, N.; Unninayar, S.; Kavvada, A.; et al. Monitoring Water-Related Ecosystems with Earth Observation Data in Support of Sustainable Development Goal (SDG) 6 Reporting. *Remote Sens.* **2020**, *12*, 1634. https://doi.org/10.3390/rs12101634.
16. Taveneau, A.; Almar, R.; Bergsma, E.W.J.; Sy, B.A.; Ndour, A.; Sadio, M.; Garlan, T. Observing and Predicting Coastal Erosion at the Langue de Barbarie Sand Spit around Saint Louis (Senegal, West Africa) through Satellite-Derived Digital Elevation Model and Shoreline. *Remote Sens.* **2021**, *13*, 2454. https://doi.org/10.3390/rs13132454.
17. Crippen, R.E. Calculating the vegetation index faster. *Remote Sens. Environ.* **1990**, *34*, 71–73. https://doi.org/10.1016/0034-4257(90)90085-Z.
18. Li, J.; Lewis, J.; Rowland, J.; Tappan, G.; Tieszen, L. Evaluation of land performance in Senegal using multi-temporal NDVI and rainfall series. *J. Arid Environ.* **2004**, *59*, 463–480. https://doi.org/10.1016/j.jaridenv.2004.03.019.
19. Lemenkova, P.; Debeir, O. Computing Vegetation Indices from the Satellite Images Using GRASS GIS Scripts for Monitoring Mangrove Forests in the Coastal Landscapes of Niger Delta, Nigeria. *J. Mar. Sci. Eng.* **2023**, *11*, 871. https://doi.org/10.3390/jmse11040871.
20. Ruan, L.; Yan, M.; Zhang, L.; Fan, X.S.; Yang, H. Spatial-temporal NDVI pattern of global mangroves: A growing trend during 2000–2018. *Sci. Total Environ.* **2022**, *844*, 157075. https://doi.org/10.1016/j.scitotenv.2022.157075.
21. Campos, J.C.; Brito, J.C. Mapping underrepresented land cover heterogeneity in arid regions: The Sahara-Sahel example. *ISPRS J. Photogramm. Remote Sens.* **2018**, *146*, 211–220. https://doi.org/10.1016/j.isprsjprs.2018.09.012.

22. Syifa, M.; Park, S.J.; Lee, C.W. Detection of the Pine Wilt Disease Tree Candidates for Drone Remote Sensing Using Artificial Intelligence Techniques. *Engineering* **2020**, *6*, 919–926. https://doi.org/10.1016/j.eng.2020.07.001.
23. Budde, M.; Tappan, G.; Rowland, J.; Lewis, J.; Tieszen, L. Assessing land cover performance in Senegal, West Africa using 1-km integrated NDVI and local variance analysis. *J. Arid Environ.* **2004**, *59*, 481–498. https://doi.org/10.1016/j.jaridenv.2004.03.020.
24. Tappan, G.; Sall, M.; Wood, E.; Cushing, M. Ecoregions and land cover trends in Senegal. *J. Arid Environ.* **2004**, *59*, 427–462. https://doi.org/10.1016/j.jaridenv.2004.03.018.
25. Deans, J.; Diagne, O.; Nizinski, J.; Lindley, D.; Seck, M.; Ingleby, K.; Munro, R. Comparative growth, biomass production, nutrient use and soil amelioration by nitrogen-fixing tree species in semi-arid Senegal. *For. Ecol. Manag.* **2003**, *176*, 253–264. https://doi.org/10.1016/S0378-1127(02)00296-7.
26. Cabral, A.I.; Costa, F.L. Land cover changes and landscape pattern dynamics in Senegal and Guinea Bissau borderland. *Appl. Geogr.* **2017**, *82*, 115–128. https://doi.org/10.1016/j.apgeog.2017.03.010.
27. Conchedda, G.; Durieux, L.; Mayaux, P. An object-based method for mapping and change analysis in mangrove ecosystems. *ISPRS J. Photogramm. Remote Sens.* **2008**, *63*, 578–589. https://doi.org/10.1016/j.isprsjprs.2008.04.002.
28. Silva, J.; Bacao, F.; Caetano, M. Specific Land Cover Class Mapping by Semi-Supervised Weighted Support Vector Machines. *Remote Sens.* **2017**, *9*, 181. https://doi.org/10.3390/rs9020181.
29. Samasse, K.; Hanan, N.P.; Anchang, J.Y.; Diallo, Y. A High-Resolution Cropland Map for the West African Sahel Based on High-Density Training Data, Google Earth Engine, and Locally Optimized Machine Learning. *Remote Sens.* **2020**, *12*, 1436. https://doi.org/10.3390/rs12091436.
30. Stoorvogel, J.; Kempen, B.; Heuvelink, G.; de Bruin, S. Implementation and evaluation of existing knowledge for digital soil mapping in Senegal. *Geoderma* **2009**, *149*, 161–170. https://doi.org/10.1016/j.geoderma.2008.11.039.
31. Pérez-Hoyos, A.; Udías, A.; Rembold, F. Integrating multiple land cover maps through a multi-criteria analysis to improve agricultural monitoring in Africa. *Int. J. Appl. Earth Obs. Geoinf.* **2020**, *88*, 102064. https://doi.org/10.1016/j.jag.2020.102064.
32. Brandt, M.; Hiernaux, P.; Rasmussen, K.; Mbow, C.; Kergoat, L.; Tagesson, T.; Ibrahim, Y.Z.; Wélé, A.; Tucker, C.J.; Fensholt, R. Assessing woody vegetation trends in Sahelian drylands using MODIS based seasonal metrics. *Remote Sens. Environ.* **2016**, *183*, 215–225. https://doi.org/10.1016/j.rse.2016.05.027.
33. Lemenkova, P. Handling Dataset with Geophysical and Geological Variables on the Bolivian Andes by the GMT Scripts. *Data* **2022**, *7*, 74. https://doi.org/10.3390/data7060074.
34. Duncan, C.; Owen, H.J.F.; Thompson, J.R.; Koldewey, H.J.; Primavera, J.H.; Pettorelli, N. Satellite remote sensing to monitor mangrove forest resilience and resistance to sea level rise. *Methods Ecol. Evol.* **2018**, *9*, 1837–1852. https://doi.org/10.1111/2041-210X.12923.
35. Lemenkova, P.; Debeir, O. Multispectral Satellite Image Analysis for Computing Vegetation Indices by R in the Khartoum Region of Sudan, Northeast Africa. *J. Imaging* **2023**, *9*, 98. https://doi.org/10.3390/jimaging9050098.
36. Purkis, S.; Klemas, V. Monitoring changes in global vegetation cover. In *Remote Sensing and Global Environmental Change*; John Wiley & Sons Ltd.: Hoboken, NJ, USA, 2011; Chapter 5, pp. 63–90. https://doi.org/10.1002/9781118687659.ch5.
37. Lemenkova, P.; Debeir, O. Recognizing the Wadi Fluvial Structure and Stream Network in the Qena Bend of the Nile River, Egypt, on Landsat 8-9 OLI Images. *Information* **2023**, *14*, 249. https://doi.org/10.3390/info14040249.
38. Diouf, A.; Lambin, E. Monitoring land-cover changes in semi-arid regions: Remote sensing data and field observations in the Ferlo, Senegal. *J. Arid Environ.* **2001**, *48*, 129–148. https://doi.org/10.1006/jare.2000.0744.
39. Suomalainen, J.; Oliveira, R.A.; Hakala, T.; Koivumäki, N.; Markelin, L.; Näsi, R.; Honkavaara, E. Direct reflectance transformation methodology for drone-based hyperspectral imaging. *Remote Sens. Environ.* **2021**, *266*, 112691. https://doi.org/10.1016/j.rse.2021.112691.
40. Olson, D.; Anderson, J. Review on unmanned aerial vehicles, remote sensors, imagery processing, and their applications in agriculture. *Agron. J.* **2021**, *113*, 971–992. https://doi.org/10.1002/agj2.20595.
41. Lemenkova, P.; Debeir, O. Satellite Image Processing by Python and R Using Landsat 9 OLI/TIRS and SRTM DEM Data on Côte d'Ivoire, West Africa. *J. Imaging* **2022**, *8*, 317. https://doi.org/10.3390/jimaging8120317.
42. Ali, I.; Cawkwell, F.; Dwyer, E.; Barrett, B.; Green, S. Satellite remote sensing of grasslands: From observation to management. *J. Plant Ecol.* **2016**, *9*, 649–671. https://doi.org/10.1093/jpe/rtw005.
43. Olson, D.; Chatterjee, A.; Franzen, D.W.; Day, S.S. Relationship of Drone-Based Vegetation Indices with Corn and Sugarbeet Yields. *Agron. J.* **2019**, *111*, 2545–2557. https://doi.org/10.2134/agronj2019.04.0260.
44. Lemenkova, P.; Debeir, O. R Libraries for Remote Sensing Data Classification by k-means Clustering and NDVI Computation in Congo River Basin, DRC. *Appl. Sci.* **2022**, *12*, 12554. https://doi.org/10.3390/app122412554.
45. Puertas, O.L.; Brenning, A.; Meza, F.J. Balancing misclassification errors of land cover classification maps using support vector machines and Landsat imagery in the Maipo river basin (Central Chile, 1975–2010). *Remote Sens. Environ.* **2013**, *137*, 112–123. https://doi.org/10.1016/j.rse.2013.06.003.
46. Petropoulos, G.P.; Kontoes, C.; Keramitsoglou, I. Burnt area delineation from a uni-temporal perspective based on Landsat TM imagery classification using Support Vector Machines. *Int. J. Appl. Earth Obs. Geoinf.* **2011**, *13*, 70–80. https://doi.org/10.1016/j.jag.2010.06.008.

47. Anees, S.A.; Mehmood, K.; Khan, W.R.; Sajjad, M.; Alahmadi, T.A.; Alharbi, S.A.; Luo, M. Integration of machine learning and remote sensing for above ground biomass estimation through Landsat-9 and field data in temperate forests of the Himalayan region. *Ecol. Inform.* **2024**, *82*, 102732. https://doi.org/10.1016/j.ecoinf.2024.102732.
48. Ibrahim, S.; Balzter, H.; Tansey, K. Machine learning feature importance selection for predicting aboveground biomass in African savannah with landsat 8 and ALOS PALSAR data. *Mach. Learn. Appl.* **2024**, *16*, 100561. https://doi.org/10.1016/j.mlwa.2024.100561.
49. Wood, E.; Tappan, G.; Hadj, A. Understanding the drivers of agricultural land use change in south-central Senegal. *J. Arid Environ.* **2004**, *59*, 565–582. https://doi.org/10.1016/j.jaridenv.2004.03.022.
50. Elberling, B.; Touré, A.; Rasmussen, K. Changes in soil organic matter following groundnut–millet cropping at three locations in semi-arid Senegal, West Africa. *Agric. Ecosyst. Environ.* **2003**, *96*, 37–47. https://doi.org/10.1016/S0167-8809(03)00010-0.
51. Hiraldo, R. Experiencing primitive accumulation as alienation: Mangrove forest privatization, enclosures and the everyday adaptation of bodies to capital in rural Senegal. *J. Agrar. Chang.* **2018**, *18*, 517–535. https://doi.org/10.1111/joac.12247.
52. Liu, S.; Kairé, M.; Wood, E.; Diallo, O.; Tieszen, L. Impacts of land use and climate change on carbon dynamics in south-central Senegal. *J. Arid Environ.* **2004**, *59*, 583–604. https://doi.org/10.1016/j.jaridenv.2004.03.023.
53. Tschakert, P.; Tappan, G. The social context of carbon sequestration: Considerations from a multi-scale environmental history of the Old Peanut Basin of Senegal. *J. Arid Environ.* **2004**, *59*, 535–564. https://doi.org/10.1016/j.jaridenv.2004.03.021.
54. Lufafa, A.; Bolte, J.; Wright, D.; Khouma, M.; Diedhiou, I.; Dick, R.; Kizito, F.; Dossa, E.; Noller, J. Regional carbon stocks and dynamics in native woody shrub communities of Senegal's Peanut Basin. *Agric. Ecosyst. Environ.* **2008**, *128*, 1–11. https://doi.org/10.1016/j.agee.2008.04.013.
55. Camara, A.; Hardy, K.; Dioh, E.; Gueye, M.; Piqué, R.; Carré, M.; Sall, M.; Diouf, M.W. Amas et sites coquilliers du delta du Saloum (Sénégal): Passé et présent. *L'Anthropologie* **2017**, *121*, 204–214. https://doi.org/10.1016/j.anthro.2017.03.018.
56. Paturel, J.E.; Mahé, G.; Diello, P.; Barbier, B.; Dezetter, A.; Dieulin, C.; Karambiri, H.; Yacouba, H.; Maiga, A. Using land cover changes and demographic data to improve hydrological modeling in the Sahel. *Hydrol. Process.* **2017**, *31*, 811–824. https://doi.org/10.1002/hyp.11057.
57. Lemenkova, P. Mapping Climate Parameters over the Territory of Botswana Using GMT and Gridded Surface Data from TerraClimate. *ISPRS Int. J. Geo-Inf.* **2022**, *11*, 473. https://doi.org/10.3390/ijgi11090473.
58. Fritz, S.; You, L.; Bun, A.; See, L.; McCallum, I.; Schill, C.; Perger, C.; Liu, J.; Hansen, M.; Obersteiner, M. Cropland for sub-Saharan Africa: A synergistic approach using five land cover data sets. *Geophys. Res. Lett.* **2011**, *38*, 1–6. https://doi.org/10.1029/2010GL046213.
59. Lemenkova, P. A GRASS GIS Scripting Framework for Monitoring Changes in the Ephemeral Salt Lakes of Chotts Melrhir and Merouane, Algeria. *Appl. Syst. Innov.* **2023**, *6*, 61. https://doi.org/10.3390/asi6040061.
60. Mbow, C.; Mertz, O.; Diouf, A.; Rasmussen, K.; Reenberg, A. The history of environmental change and adaptation in eastern Saloum–Senegal—Driving forces and perceptions. *Glob. Planet. Chang.* **2008**, *64*, 210–221. https://doi.org/10.1016/j.gloplacha.2008.09.008.
61. Ndour, A.; Laïbi, R.A.; Sadio, M.; Degbe, C.G.; Diaw, A.T.; Oyédé, L.M.; Anthony, E.J.; Dussouillez, P.; Sambou, H.; Hadji Balla Dièye, E. Management strategies for coastal erosion problems in west Africa: Analysis, issues, and constraints drawn from the examples of Senegal and Benin. *Ocean Coast. Manag.* **2018**, *156*, 92–106. https://doi.org/10.1016/j.ocecoaman.2017.09.001.
62. Ngom, F.; Tweed, S.; Bader, J.C.; Saos, J.L.; Malou, R.; Leduc, C.; Leblanc, M. Rapid evolution of water resources in the Senegal delta. *Glob. Planet. Chang.* **2016**, *144*, 34–47. https://doi.org/10.1016/j.gloplacha.2016.07.002.
63. Lombard, F.; Soumaré, S.; Andrieu, J.; Josselin, D. Mangrove zonation mapping in West Africa, at 10-m resolution, optimized for inter-annual monitoring. *Ecol. Inform.* **2023**, *75*, 102027. https://doi.org/10.1016/j.ecoinf.2023.102027.
64. Carney, J.; Gillespie, T.W.; Rosomoff, R. Assessing forest change in a priority West African mangrove ecosystem: 1986–2010. *Geoforum* **2014**, *53*, 126–135. https://doi.org/10.1016/j.geoforum.2014.02.013.
65. Andrieu, J.; Lombard, F.; Fall, A.; Thior, M.; Ba, B.D.; Dieme, B.E.A. Botanical field-study and remote sensing to describe mangrove resilience in the Saloum Delta (Senegal) after 30 years of degradation narrative. *For. Ecol. Manag.* **2020**, *461*, 117963. https://doi.org/10.1016/j.foreco.2020.117963.
66. Devaney, J.L.; Marone, D.; McElwain, J.C. Impact of soil salinity on mangrove restoration in a semiarid region: a case study from the Saloum Delta, Senegal. *Restor. Ecol.* **2021**, *29*, e13186. https://doi.org/10.1111/rec.13186.
67. Neteler, M.; Beaudette, D.E.; Cavallini, P.; Lami, L.; Cepicky, J., GRASS GIS. In *Open Source Approaches in Spatial Data Handling*; Springer Berlin Heidelberg: Berlin/Heidelberg, Germany, 2008; pp. 171–199. https://doi.org/10.1007/978-3-540-74831-1_9.
68. Wessel, P.; Luis, J.F.; Uieda, L.; Scharroo, R.; Wobbe, F.; Smith, W.H.F.; Tian, D. The Generic Mapping Tools Version 6. *Geochem. Geophys. Geosyst.* **2019**, *20*, 5556–5564. https://doi.org/10.1029/2019GC008515.
69. Lemenkova, P.; Debeir, O. Coherence of Bangui Magnetic Anomaly with Topographic and Gravity Contrasts across Central African Republic. *Minerals* **2023**, *13*, 604. https://doi.org/10.3390/min13050604.
70. Lemenkova, P. Mapping submarine geomorphology of the Philippine and Mariana trenches by an automated approach using GMT scripts. *Proc. Latv. Acad. Sci. Sect. B Nat. Exact Appl. Sci.* **2022**, *76*, 258–266. https://doi.org/10.2478/prolas-2022-0039.
71. Lemenkova, P. Tanzania Craton, Serengeti Plain and Eastern Rift Valley: Mapping of geospatial data by scripting techniques. *Est. J. Earth Sci.* **2022**, *71*, 61–79. https://doi.org/10.3176/earth.2022.05.

72. Lemenkova, P. Cartographic scripts for seismic and geophysical mapping of Ecuador. *Geografie* **2022**, *127*, 195–218. https://doi.org/10.37040/geografie.2022.006.
73. Neteler, M.; Bowman, M.H.; Landa, M.; Metz, M. GRASS GIS: A multi-purpose open source GIS. *Environ. Model. Softw.* **2012**, *31*, 124–130. https://doi.org/10.1016/j.envsoft.2011.11.014.
74. Neteler, M.; Mitasova, H. *Open Source GIS—A GRASS GIS Approach*, 3rd ed.; Springer: New York, NY, USA, 2008.
75. Woomer, P.; Tieszen, L.; Tappan, G.; Touré, A.; Sall, M. Land use change and terrestrial carbon stocks in Senegal. *J. Arid Environ.* **2004**, *59*, 625–642. https://doi.org/10.1016/j.jaridenv.2004.03.025.
76. Carney, J. "The mangrove preserves life": Habitat of African survival in the Atlantic world. *Geogr. Rev.* **2017**, *107*, 433–451. https://doi.org/10.1111/j.1931-0846.2016.12205.x.
77. Galat-Luong, A.; Galat, G. La colonisation de la mangrove par Cercopithecus aethiops sabaeus au Sénégal. *Rev. Écol.* **1976**, *30*, 3–30. https://doi.org/10.3406/revec.1976.4910.
78. Faye, B.; Du, G. Agricultural Land Transition in the "Groundnut Basin" of Senegal: 2009 to 2018. *Land* **2021**, *10*, 996. https://doi.org/10.3390/land10100996.
79. Branoff, B.L. Quantifying the influence of urban land use on mangrove biology and ecology: A meta-analysis. *Glob. Ecol. Biogeogr.* **2017**, *26*, 1339–1356. https://doi.org/10.1111/geb.12638.
80. Robequain, C. La végétation du Sénégal. *Ann. Géogr.* **1942**, *51*, 293–297. https://doi.org/10.3406/geo.1942.12096.
81. Manlay, R.J.; Cadet, P.; Thioulouse, J.; Chotte, J.L. Relationships between abiotic and biotic soil properties during fallow periods in the sudanian zone of Senegal. *Appl. Soil Ecol.* **2000**, *14*, 89–101. https://doi.org/10.1016/S0929-1393(00)00052-4.
82. Bennour, A.; Jia, L.; Menenti, M.; Zheng, C.; Zeng, Y.; Barnieh, B.A.; Jiang, M. Assessing impacts of climate variability and land use/land cover change on the water balance components in the Sahel using Earth observations and hydrological modelling. *J. Hydrol. Reg. Stud.* **2023**, *47*, 101370. https://doi.org/10.1016/j.ejrh.2023.101370.
83. Brandt, M.; Grau, T.; Mbow, C.; Samimi, C. Modeling Soil and Woody Vegetation in the Senegalese Sahel in the Context of Environmental Change. *Land* **2014**, *3*, 770–792. https://doi.org/10.3390/land3030770.
84. Mazzero, H.; Perrotton, A.; Ka, A.; Goffner, D. Unpacking Decades of Multi-Scale Events and Environment-Based Development in the Senegalese Sahel: Lessons and Perspectives for the Future. *Land* **2021**, *10*, 755. https://doi.org/10.3390/land10070755.
85. Furian, S.; Mohamedou, A.O.; Hammecker, C.; Maeght, J.L.; Barbiero, L. Soil cover and landscape evolution in the Senegal floodplain: A review and synthesis of processes and interactions during the late Holocene. *Eur. J. Soil Sci.* **2011**, *62*, 902–912. https://doi.org/10.1111/j.1365-2389.2011.01398.x.
86. Lézine, A.M. Evolution of the West African Mangrove During the Late Quaternary: A Review. *Géogr. Phys. Quat.* **1997**, *51*, 405–414. https://doi.org/10.7202/033139ar.
87. Loum, M.; Viaud, V.; Fouad, Y.; Nicolas, H.; Walter, C. Retrospective and prospective dynamics of soil carbon sequestration in Sahelian agrosystems in Senegal. *J. Arid. Environ.* **2014**, *100–101*, 100–105. https://doi.org/10.1016/j.jaridenv.2013.10.007.
88. Brink, A.B.; Eva, H.D. Monitoring 25 years of land cover change dynamics in Africa: A sample based remote sensing approach. *Appl. Geogr.* **2009**, *29*, 501–512. https://doi.org/10.1016/j.apgeog.2008.10.004.
89. Dièye, E.; Diaw, A.; Sané, T.; Ndour, N. Dynamique de la mangrove de l'estuaire du Saloum (Sénégal) entre 1972 et 2010. Dynamics of the Saloum estuary mangrove (Senegal) from 1972 to 2010. *Cybergeo Eur. J. Geogr. Environ. Nat. Paysage* **2013**, *629*, 1–26.
90. Lebigre, J.M. La dynamique des mangroves à travers leurs lisières: Éléments de diagnostic. *Trav. Lab. Géogr. Phys. Appl.* **1998**, *17*, 65–76. https://doi.org/10.3406/tlgpa.1998.957.
91. Diaw, T.; Loubersac, L.; Belbeoch, G. L'analyse des données Spot simulées sur les marais tropicaux. L'exemple des îles du Saloum (Sénégal). *Bull. Assoc. Géogr. Français* **1982**, *59*, 293–295. https://doi.org/10.3406/bagf.1982.5370.
92. Lombard, F.; Andrieu, J. Mapping Mangrove Zonation Changes in Senegal with Landsat Imagery Using an OBIA Approach Combined with Linear Spectral Unmixing. *Remote Sens.* **2021**, *13*, 1961. https://doi.org/10.3390/rs13101961.
93. Fent, A.; Bardou, R.; Carney, J.; Cavanaugh, K. Transborder political ecology of mangroves in Senegal and The Gambia. *Glob. Environ. Chang.* **2019**, *54*, 214–226. https://doi.org/10.1016/j.gloenvcha.2019.01.003.
94. Bourgoin, J.; Valette, E.; Guillouet, S.; Diop, D.; Dia, D. Improving Transparency and Reliability of Tenure Information for Improved Land Governance in Senegal. *Land* **2019**, *8*, 42. https://doi.org/10.3390/land8030042.
95. Kalema, V.N.; Witkowski, E.T.F.; Erasmus, B.F.N.; Mwavu, E.N. The Impacts of Changes in Land Use on Woodlands in an Equatorial African Savanna. *Land Degrad. Dev.* **2015**, *26*, 632–641. https://doi.org/10.1002/ldr.2279.